



## Livrable 8.2 CONSTRUCTION ARBRE DE DECISION

Auteur : Jean-Robert Grasso, ISTerre

### INTRODUCTION

#### SCENARISATION DE LA MENACE OU COMMENT GERER L'INCERTAIN.

La stratégie mise en œuvre dans le projet SLAMS vise à construire de nouveaux outils (prototypes expérimentaux, outils numériques, modèles au sens large) qui permettent de fournir une plateforme d'aide à la décision pour des estimations quantitatives de l'aléa mouvement gravitaire sur le site de Séchilienne. Pour atteindre cet objectif, une partie de la tache 8 tend vers une synthèse des différentes étapes du projet SLAMS, qui vise à analyser et identifier chaque pas du processus de cascade dans la chaîne d'événements d'où peut émerger la propagation catastrophique d'une pente instable. A chaque pas de la chaîne d'événements qui constituent une cascade, on s'attache à quantifier les erreurs relatives tant aux types de données (aléatoires) qu'aux manques de connaissance sur les processus impliqués (épistémiques).

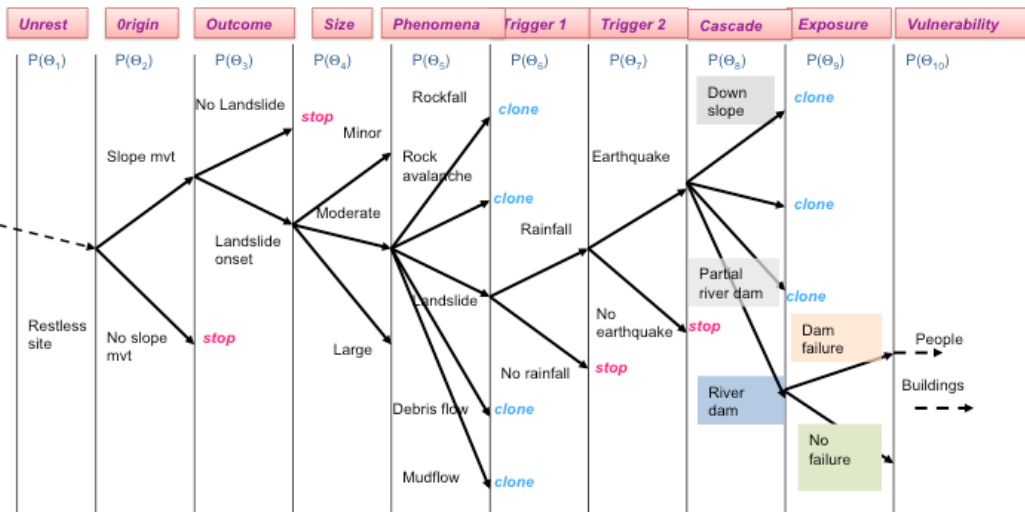
Cette « pluri-disciplinarité » entre sismologie, géomorphologie, hydrologie, mécanique des roches et géologie est nécessaire pour une approche croisée indispensable à la compréhension du déclenchement des instabilités gravitaires.

D'un point de vue global, ce livrable interroge les bases qui ont servies à structurer le processus de décision associé au forçage du mouvement de terrain sur les pentes de Séchilienne par un séisme et du lac barrage qui pourrait y être associé. Ces interrogations, basées sur une analyse des processus d'interactions séismes - mouvement de terrain tant au niveau régional (Grasso et al., 2014) qu'au niveau mondial (Tatard et Grasso, 2013). Dans le contexte de la question de la décision en univers incertain, nous avons privilégié l'approche probabiliste en prenant en analysant des comportements moyens tant au niveau mondial qu'au niveau des alpes françaises.

Si l'objectif initial de ce livrable s'appuyait sur la synthèse des résultats des différentes taches, les retards dans certaines taches en amont de notre contribution n'ont pas permis la réalisation d'un arbre de décision quantitatif complet, depuis un déplacement initial de quelques cibles « au-delà de la normale », jusqu'à la propagation d'un volume dont la taille est issue d'une loi de distribution et qui se propage à une distance dont la variabilité correspondant à différentes simulations (données probabilistes), cet éboulement créant un possible barrage, ce dernier rompant avec une probabilité temporelle (Figure 1). Dans ce contexte, nos travaux se sont donc concentrés sur

- l'évaluation de susceptibilité de la pente de Séchilienne à un séisme ;
- la probabilité de rupture d'un éventuel barrage;

Decision tree prototype:



⇒ To quantify each  $P(\Theta_j)$ , identifying a non uniform fonctionnal

**Figure 1 :** Schéma de principe d'un prototype d'arbre de décision pour les mouvements de terrains déclenchés par les séismes. Chaque sous ensemble de ces étapes est aussi abordé via un arbre de décision spécifique non détaillé ici.

Le travail entrepris est donc articulé autour de 3 activités scientifiques distinctes que nous avons souhaitées les plus complémentaires possibles:

- approche probabiliste sur des phases clefs de la cascade d'évènement qui mènent à une catastrophe dite naturelle (prototype d'arbre de décision) ;
- mesure probabiliste de la susceptibilité aux séismes des pentes de Séchilienne dans le contexte alpin ;
- probabilité de rupture d'un lac - barrage post effondrement

## Interactions séismes mouvements de terrains : implications dans le contexte du glissement lent de Séchilienne

### 1- Enjeux et problématiques, état de l'art:

Les glissements de terrain sont la cause principale des dommages (en structures et personnes) induits par les séismes en zone de montagne. L'impact des glissements de terrains déclenchés par un séisme dans les Alpes françaises, dans un contexte de pentes fortes et sismicité modérée, n'est actuellement pas analysé ni connu. Dans le contexte spécifique de l'impact de sollicitations sismiques sur des glissements actifs lents (cm au m par an ; cas de Séchilienne), la susceptibilité

d'une pente alpine en mouvement lent à une sollicitation sismique ainsi que la cascade associée (séisme - mouvement de terrain - lac/barrage - rupture/barrage) n'est pas quantifiée. Parmi les éléments qui contribuent à cette lacune on notera :

- l'absence d'évènement catastrophique contemporain (localement rupture d'un barrage-lac après éboulement en 1149, 20 km en amont de Séchilienne (Rochetaillée) ;
- le retard/compétence de la communauté française sur les études d'interactions séismes mouvement de terrain et dans la moindre mesure, communauté européenne (exception partielle pour l'Italie et l'Espagne) ;
- la sous-évaluation de la susceptibilité au séisme pour Séchilienne, couplé au rejet de la rupture du barrage - lac, par la commission d'expert (rapport Panet 2003-2009) sans argumentation pour les réponses aux séismes et sur la base d'expérience de laboratoire pour la rupture du barrage.

Dans le contexte international, les mécanismes de déclenchement pour différents cas mondiaux restent peu compris malgré l'acquisition récente de données denses et robustes. Les contributions scientifiques dans ce domaine se focalisent sur :

- la réalisation de carte de susceptibilité aux séismes, analyses rétrospectives, non validées en prospectif. On citera l'exception en cours en Nouvelle Zélande où une carte de susceptibilité prospective, pour la faille Alpine (NZ) est en cours de réalisation à l'aide de la base de données des glissements déclenchés en Chine par le séisme du Sichuan, (2008), (T. Davies, communication personnelle 2013, Davies 2013)
- la construction de lois empiriques, du type distance maximale de déclenchement en fonction de la magnitude du séisme déclencheur (pour une analyse globale, Keefer 2002).

De nombreuses études privilégièrent le rôle du terrain (pente, roche) en lien avec le forçage lié à l'accélération du mouvement du sol induite par le séisme, l'amplitude maximale étant suggérée comme privilégiée par des effets locaux (topographie, matériau), (voir par exemple Meunier et al. 2007). L'ensemble de ces études néglige l'influence de la cinématique de la source sismique sur les déclenchements. Dans ce contexte, nos travaux se sont donc concentrés sur

- l'évaluation de la variabilité de la susceptibilité des pentes en fonction du type de mouvement sismique à la source (effet de source), sur la base de 8 bases de données mondiales pour des séismes déclencheurs entre des magnitudes  $M_w = 5.6-8.0$ . Cette gamme de magnitude correspond à des tailles de failles ayant glissées lors du séisme dans la gamme  $L=4-200$  km (Tatard et Grasso, 2013)
- l'évaluation de la variabilité de la susceptibilité des pentes en fonction de la taille du séisme déclencheur dans le contexte alpin, sur la base des 5 inventaires les plus robustes dans le contexte des alpes françaises (séismes déclencheurs entre des magnitudes  $M_w = 4.5-6.0$ , dans la période 1900-2010).
- l'évaluation de la probabilité de rupture d'un éventuel barrage. On a ici utilisé les observations existantes dans le contexte des lac-barrages induits par le séisme de Wenchuan, Chine, 2008 ainsi que les synthèses mondiales existantes (Fan et al 2012 ; Rodriguez et al . 1999)

## **2- le rôle du glissement co-sismique (amplitude et orientation) comme paramètre de contrôle des distances d'interactions séismes glissement de terrains**

Pour quantifier le rôle du glissement sismique dans les interactions séisme - glissement de terrain, on a dans un premier temps caractérisé le comportement moyen de 8 séquences mondiales majeures de glissements de terrains déclenchés par des séismes, dans la gamme de magnitudes  $M_w = 5.6-8.0$ . Ces comportements moyens permettent d'analyser les distributions des distances des glissements de terrains par rapport à la faille sismique (figure 2). De plus, l'introduction originale de « distance normalisée » telle que distance du glissement de terrain déclenché au séisme / longueur de faille sismique, plutôt que distance à la faille sismique, permet de lisser les

effets géomorphologiques locaux en donnant accès au rôle possible de la source sismique. Cette innovation méthodologique a fait l'objet d'une publication Tatard et Grasso, 2013, Journal of Geophysical Research, solid earth, Annexe 1).

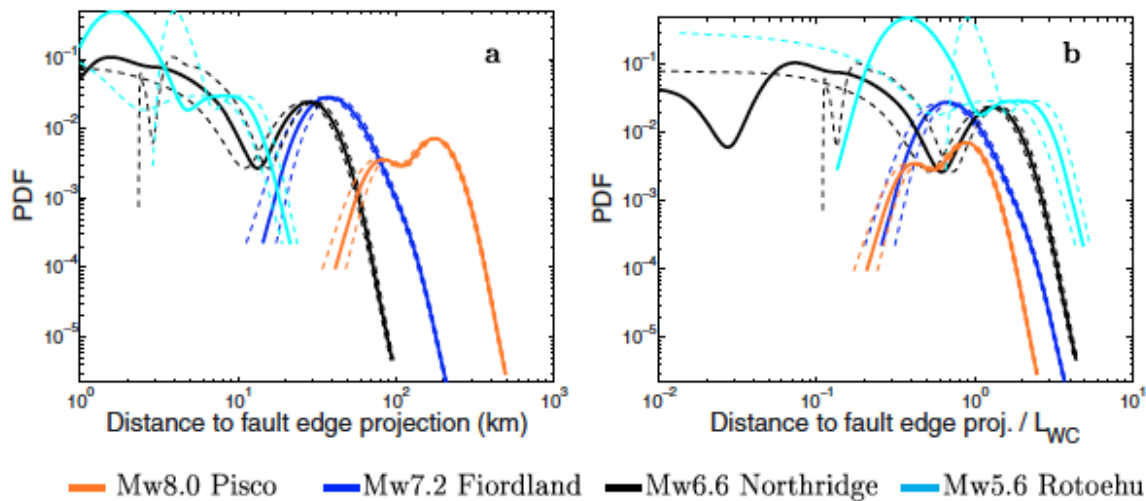


**Figure 2 :** distribution des distances à la faille pour les glissements de terrains déclenchés (hanging wall) par les 4 séismes en faille inverse, sans rupture de surface. (b) En utilisant les distances normalisées, les distances maximales chutent à une distance indépendante de la magnitude du séisme ; cette chute démontrent le rôle de la déformation sismique dans le contrôle des distances où les mouvements de terrains sont induits (Tatard et Grasso 2013)

Cette même méthode, appliquée sur les inventaires des séismes modérés alpins pour 5 évènements de magnitudes M=4.9-6.0 (Grasso et al. 2013), suggère que la susceptibilité des pentes aux séismes en zone sismique modérée (le contexte alpin français) suit des lois semblables à celles qui caractérisent cette susceptibilité dans des contextes tectonique plus actifs. Formulées de façon différente, nos analyses ne montrent pas d'écart significatif dans les distances de déclenchements en contexte alpins, et confirment donc une forme d'universalité des distances d'interactions séismes glissement de terrains qui dépendent du mécanisme à la source du séisme (figure 3). Les inventaires actuellement disponibles, tant au niveau régional qu'au niveau mondial, ne sont pas robustes pour analyser l'impact des séismes tant en terme de nombre de glissements déclenchés qu'en terme des volumes totaux mobilisés (Tatard et Grasso, 2013).

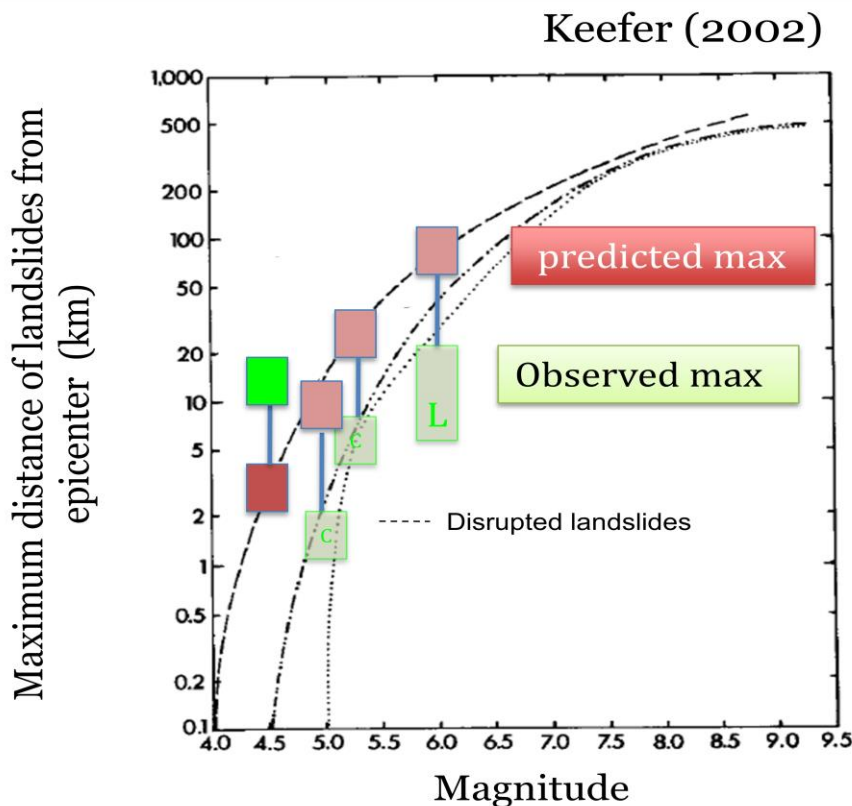


**Figure 3a :** distribution des distances à la faille pour un catalogue mondial de glissements de terrain déclenchés par des séismes.

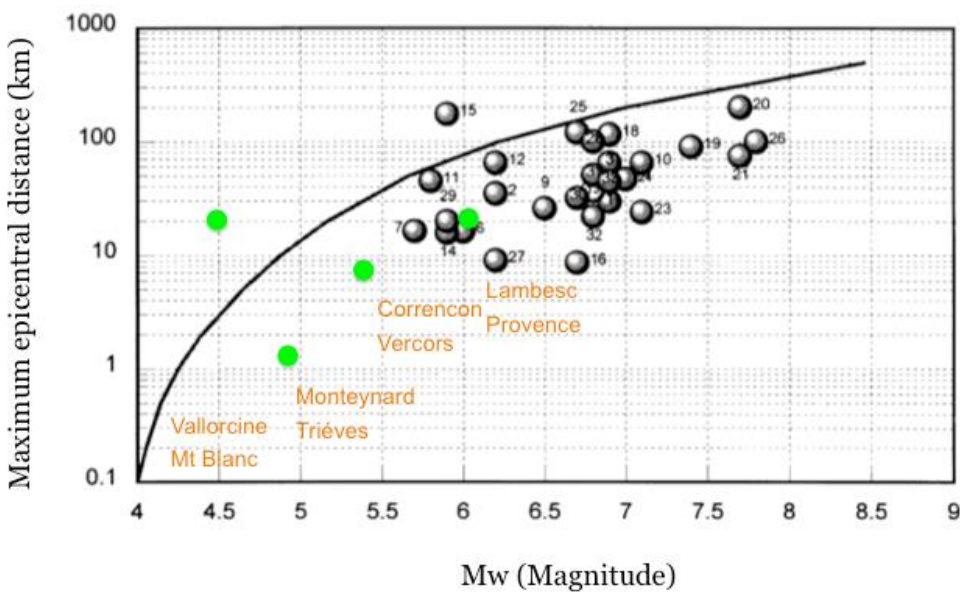


**Figure 3b :** distribution des distances à la faille pour les glissements de terrains déclenchés par 4 séismes français,  $M=6$ , 1906, Provence,  $M=5.3$ , 1962, Vercors ;  $M=4.9$ , 1963 Trièves ;  $M=4.5$ , 2005, Mont blanc). On observe que les distances maximales (verts) sont en accord avec celles observées au niveau mondiale (Rodriguez 1999) excepté pour le cas du séisme de Vallorcine (Mt Blanc 2005).

### Le cas de la stabilité des lac-barrages :

En ce qui concerne la stabilité d'un barrage consécutif au possible effondrement dans le contexte de Séchilienne, nous avons collaboré avec le groupe de Chengdu (Sichuan, Chine) leader actuel dans cette problématique. La base de données consécutive au séisme de Wenchuan (2008) permet une analyse statistique de la stabilité des 450 lac-barrages contemporains à ce séisme. Cette base de données est comparée aux bases de données mondiales (Xuanmei et al. 2012). Tant dans les cas spécifiques de déclenchements sismiques (Chine) que pour des ensembles régionaux (exemple de la Nouvelle Zélande) ou lors de la synthèse de cas mondiaux, une loi de puissance émerge comme reproduisant les durées de vies de ces lacs-barrages. Même si le calage sur les données locales, pour ce dernier aspect, est en cours via la recherche d'exemples historiques dans le contexte alpin, l'ensemble des mesures actuelles montrent une stabilité non déterministe. Cette instabilité conditionnelle est compatible avec des durées de vie en loi de puissance.

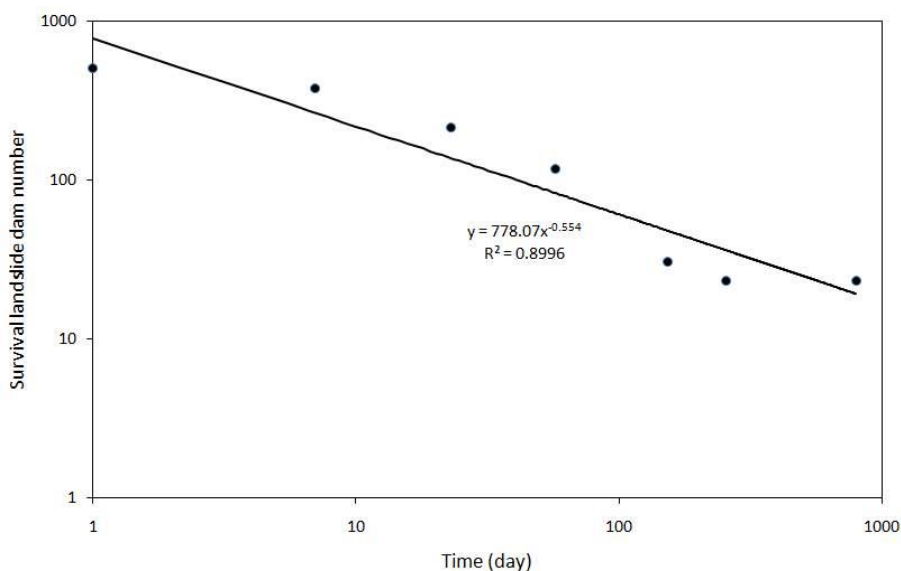


**Figure 4** : distribution des temps de survie des lac-barrages induits par le séisme du Wenchuan, chine, 2008 (adapté de Xuanmei, et al. 2012). On observe une distribution en loi de puissance, caractéristique des systèmes non prédictibles où de nombreuses interactions contrôlent la dynamique de ces systèmes (from Xuanmei et al. 2012).

### 3- Synthèse des résultats principaux

Dans le domaine des interactions séismes/mouvement de terrains (contexte des alpes françaises) nos contributions s'énoncent comme suit :

- la validation, en domaine alpin, des relations empiriques distances maximales de déclenchement en fonction de la magnitude du séisme (études des séismes contemporain significatifs des alpes françaises (5 cas 1906, 1959, 1962, 1963 2005). Ces résultats fournissent des zones d'influence des séismes pour le déclenchement de Séchilienne, en fonction de la taille du séisme. Un second résultat suggère une plus forte susceptibilité dans les alpes du nord (région de Chamonix), cette susceptibilité anormale semble être corrélée à la modification des limites des parois en zone de permafrost, due au réchauffement climatique (figure 5)

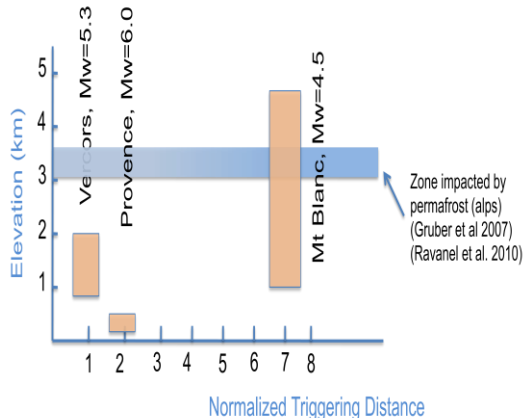


**Figure 5 :** distribution des distances à la faille pour les glissements de terrains déclenchés par 4 séismes français,  $M=6$ , 1906, Provence,  $M=5.3$ , 1962, Vercors ;  $M=4.9$ , 1963 Trièves, ;  $M=4.5$ , 2005, Mont blanc). On observe que les distances maximales de l'ordre de 1-2 fois la distance normalisée sont en accord avec les cas mondiaux (voir figure 3, et table 3) pour les séismes Vercors, Trièves et Provence. Exception pour le cas du séisme de Vallorcine (Mt Blanc 2005) qui déclenche à plus de 6 fois la longueur de faille. Cette forte susceptibilité pour cette événement est probablement du à un effet de remonté en altitude du permafrost lié au changement climatique en cours (Grasso et al. 2013). La bande bleue constitue les évaluations actuelles des zones de permafrost dans les alpes françaises telles que définies par Gruber et al (2007), Ravanel et al. (2010)

- mise en évidence du rôle de la cinématique de la source sismique dans le contrôle des distances de déclenchement à partir d'inventaires mondiaux bien contraints. Ces résultats permettent d'affiner les résultats précédents en fonction du style de déformation sismique (faille inverse, normale ou coulissage)
- à partir des deux contributions précédentes une gamme de distance normalisée séisme - pente où un pourcentage donné de glissement de terrain est localisé ; les applications à Séchilienne sont dérivées pour différents types et magnitudes de séismes (voir table ci dessous).

**Table 3.  $d_{95}^*$  and  $d_{75}^*$  Normalized Distances for All Earthquakes<sup>a</sup>**

Earthquake Focal Mechanism	Catalog	$d_{95}^*$	$d_{75}^*$	$d_{95\text{-}\%DS}^*$	$d_{75\text{-}\%DS}^*$
Surface-faulting earthquakes	Wenchuan	0.7	0.1	0.4	0.1
	Chi-Chi	0.8	0.2	0.8	0.2
	Kashmir	0.5	0.1	0.4	0.1
	Mean	0.7	0.1	0.5	0.1
Buried, oblique-slip earthquake	Loma Prieta	1.0	0.3	2.3	0.6
Buried, dip-slip earthquakes	Fiordland	3.2	1.9	3.2	1.9
	Northridge	2.9	0.7	2.9	0.7
	Rotoehu	4.1	1.9	4.1	1.9
	Pisco	2.2	1.3	2.2	1.3
	Mean	3.1	1.5	3.1	1.5

<sup>a</sup> $d_{95}$  and  $d_{75}$  are the distances normalized by LWC at which 95 and 75% of the landslides occurred, respectively.  $d_{95\text{-}\%DS}^*$  and  $d_{75\text{-}\%DS}^*$  are the distances normalized by LWC and weighted by the strike-slip component of the coseismic slip at which 95 and 75% of the landslides occurred, respectively.

**Table 1 :** distances pour lesquelles 95% et 75% des glissements de terrains ont lieu. La moyenne par type de mécanisme au foyer montre que les séismes en failles inverses déclenchent plus loin que des

séismes avec une composante de coulissage.

Dans le contexte des lacs barrages et de leur rupture (cas Séchilienne - contexte des alpes françaises) les résultats concernent:

– le rejet d'une stabilité déterministe du barrage créée par l'effondrement éventuel de Séchilienne: une synthèse des observations des cas mondiaux, en utilisant tant les moyennes régionales (Chine, Japon, Nouvelle-Zélande) que la moyenne mondiale, démontre une instabilité stochastique récurrente de la durée de vie des barrages créés par les mouvements de terrains. L'ensemble des études suggère des durées de vie en loi de puissance pour ces types de lacs barrage. Ces études concernent des volumes,  $V < \text{km}^3$ , et donc, elles n'impliquent pas la classe de glissement « géant » telle que dénommée dans cette communauté scientifique.

#### **4-Limites actuelles**

En ce concerne les analyses concernant les cas français, le calibrage des lois de déclenchements à partir des cas historiques se fait à partir de faibles volumes ( $V < 10^3 \text{ m}^3$ ). Cette limite apparente doit être nuancée par les observations récurrentes de distributions en lois de puissances pour les tailles des glissements induits par les sollicitations sismiques. Dans un tel contexte la probabilité de déclenchement d'un gros volume est plus faible, ce qui est conforme au premier ordre à nos observations.

Une seconde limite potentielle est le calage en magnitude dans un contexte où les effets de site sur le glissement modifient les amplitudes des ondes sismiques (voir résultats sur Séchilienne dans ce rapport, livrable 1.3, Garambois et al. 2013). Un rapport d'amplitude de 10 par exemple revient à une augmentation d'une unité de magnitude. Cet effet potentiel intervenant pour l'ensemble des pentes mondiales analysées, les diagrammes magnitude-distance que nous utilisons restent inchangés en relatif, en France ou mondialement; on doit alors introduire la notion de magnitude efficace pour inclure un effet de site potentiel. Dans ce sens les lois actuelles de seuil de déclenchement minimisent l'amplitude réelle qui déclenche un séisme. Par exemple ce ne sera pas un  $M=6$  à 30 km de distance, mais plutôt une amplitude efficace,  $A_{\text{eff}} = A_{(M6)+dA}$

$dA$ , étant la correction correspondant à l'amplitude modifiée par effet de site (donc la nouvelle magnitude « efficace »  $M_{\text{eff}} = M_6 - dM$ ).

Enfin le calage des lois de rupture de barrage sur les exemples historiques en contexte alpin n'a pu être finalisé dans le temps de ce projet (en cours).

#### **5- Synthèse**

Les 2 classes de résultats décrits précédemment éCLAIRENT différemment les conclusions des rapports d'experts sur le site de Séchilienne. La synthèse en cours tente de réconcilier ces approches en situant, dans un prototype d'arbre de décision, les scenarii proposés « à dire d'expert » comparativement à un ensemble de scenarii probabilistes. Les résultats préliminaires nous permettent de fournir les éléments de synthèse suivant, à savoir que les scenarii envisagés par les entités en charge des alertes et donc du risque (telles qu'accessibles via les rapports ouverts) minimisent tant l'impact d'un séisme sur la cinématique du mouvement de Séchilienne que la possibilité de rupture du lac barrage consécutif à l'effondrement d'une partie du versant de Séchilienne. Cette minimisation est mesurée relativement aux études que nous avons effectuées à l'aide des bases de données mondiales auxquelles nous avons pu nous référer lors du projet SLAMS.

## 6- références

- Davies, T., 2013, The wenchuan co-seismic landslides –susceptibility analysis,in The International Symposium in Commemoration of the 5th Anniversary of the 2008 Wenchuan Earthquake, May 11-13 2013, Chengdu China
- Grasso JR, L. Tatard, C. Voisin, C.Sue: 2013, Earthquake triggering potency for landslides: strong topography contrast, low tectonic loading, and low weathering context (French Alps), in JAG3, 17-18 septembre 2013 Grenoble, France
- Gruber, S., & Haeberli, W. (2007). Permafrost in steep bedrock slopes and its temperature-related destabilization following climate change. *Journal of Geophysical Research: Earth Surface* (2003-2012), 112(F2).
- Keefer, D. K. (2002), Investigating landslides caused by earthquakes - a historical review, *Surv. Geophys.*, 23, 573–510.
- Meunier, P., N. Hovius, and A. J. Haines (2007), Regional patterns of earthquake-triggered landslides and their relation to ground motion. *Geophys. Res. Lett.*, 34, L20408, doi:10.1029/2007GL031337.
- Panet ; M. et al. 2003, Versant instable des ruines de séchilienne, rapport du collège d'expert, 11pp
- Panet ; M. et al. 2003, Scenarios d'évolutions du versant des ruines de séchilienne, rapport du collège d'expert.
- Ravanel L and P Deline (2010) Climate influence on rockfalls in high-Alpine steep rockwalls: The north side of the Aiguilles de Chamonix (Mont Blanc massif) since the end of the ‘Little Ice Age, *The Holocene March 2011 vol. 21 no. 2* 357-365.
- Rodriguez, C.E., Bommer, J.J. and R.J. Chandler [1999], “Earthquake-induced landslides: 1980-1997”, *Soil Dynamic Earthquake Engineering*, 18, 325-346.
- Tatard, L., and J. R. Grasso (2013), Controls of earthquake faulting style on near field landslide triggering: The role of coseismic slip, *J. Geophys. Res. Solid Earth*, 118, doi:10.1002/jgrb.50215.
- X Fan, CJ van Westen, Q Xu, T Gorum, F Dai, Analysis of landslide dams induced by the 2008 Wenchuan earthquake - *Journal of Asian Earth Sciences*, 2012.

ANNEXE : TATARD and GRASSO, 2015, *Journal of Geophysical Research*, Controls of earthquake faulting style on near field landslide triggering: The role of coseismic slip

# Controls of earthquake faulting style on near field landslide triggering: The role of coseismic slip

L. Tatard<sup>1,2</sup> and J. R. Grasso<sup>1</sup>

Received 30 August 2012; revised 7 May 2013; accepted 8 May 2013; published 17 June 2013.

[1] We compare the spatial distributions of seven databases of landslides triggered by  $M_w=5.6\text{--}7.9$  earthquakes, using distances normalized by the earthquake fault length. We show that the normalized landslide distance distributions collapse, i.e., the normalized distance distributions overlap whatever the size of the earthquake, separately for the events associated with dip-slip, buried-faulting earthquakes, and surface-faulting earthquakes. The dip-slip earthquakes triggered landslides at larger normalized distances than the oblique-slip event of Loma Prieta. We further identify that the surface-faulting earthquakes of Wenchuan, Chi-Chi, and Kashmir triggered landslides at normalized distances smaller than the ones expected from their  $M_w \geq 7.6$  magnitudes. These results support a control of the seismic slip (through amplitude, rake, and surface versus buried slip) on the distances at which landslides are triggered. In terms of coseismic landslide management in mountainous areas, our results allow us to propose distances at which 95 and 75% of landslides will be triggered as a function of the earthquake focal mechanism.

**Citation:** Tatard, L., and J. R. Grasso (2013), Controls of earthquake faulting style on near field landslide triggering: The role of coseismic slip, *J. Geophys. Res. Solid Earth*, 118, 2953–2964, doi:10.1002/jgrb.50215.

## 1. Introduction

[2] Interactions between earthquakes and landslides are currently analyzed either from a triggering factor approach, i.e., the ground motions generated by the earthquake faulting, or from a conditioning factor approach, i.e., the geometry of the slope and its material properties. While numerous studies aim to quantify the control of the geology and geomorphology parameters on the spatial distribution of landslides [e.g., Parise and Jibson, 2000; Keefer, 2000; Murphy *et al.*, 2002; Hancox *et al.*, 2003, 2004; Sepúlveda *et al.*, 2005; Sato *et al.*, 2007; Kamp *et al.*, 2008; Jinhuin *et al.*, 2010; Dai *et al.*, 2010; Lee, 2010], a few focus on the possible seismic ground motion thresholds for landslide onset [Keefer, 2002; Khazai and Sitar, 2004; Dadson *et al.*, 2004; Meunier *et al.*, 2007]. The seismic ground motions recorded at a given slope are the convolution of (i) the earthquake source effect, which corresponds to the nucleation and propagation of the seismic slip and generation of seismic waves; (ii) a path effect, which corresponds to the modification of the emitted wave field by the crust heterogeneities during its propagation toward the target site; and (iii) a site effect, which corresponds to the possible local amplification by the topography and/or the geology of

the emitted wave field at a given frequency. Keefer [2002] gives empirical landslide triggering thresholds from Arias intensity values (a function of ground acceleration and duration notably), depending on the landslide types. Khazai and Sitar [2004] showed a qualitative agreement between the landslide locations and the iso-values of peak ground acceleration (PGA), for the  $M_w=7.6$  Chi-Chi landslides. Dadson *et al.* [2004] showed a linear relationship between the area affected by landsliding and the vertical component of the PGA for the Chi-Chi earthquake, while Meunier *et al.* [2007] showed a linear relationship between the density of coseismic landslides and both the vertical and horizontal components of the PGA for the  $M_w=7.6$  Chi-Chi and the  $M_w=6.6$  Northridge earthquakes. While these peak ground motion values may be efficient to predict landslide occurrences, they are related to a single value of the ground motion. A comprehensive analysis of the influence of the whole ground motion on landslide triggering is not yet available.

[3] On the other hand, Keefer [2002] showed that landslide maximum triggering distances scale with the earthquake magnitude, which suggests a direct control of the earthquake source mechanics on landslide triggering. Also, Gorum *et al.* [2011] highlighted a qualitative correlation between landslide distribution and earthquake source mechanics, as the coseismic slip distribution and the fault geometry, for the Wenchuan earthquake.

[4] To capture how the earthquake source mechanics may interact with landslide occurrences close to the earthquake fault, the seismic source can be broken down as a two-step process [e.g., Sibson, 2002]: (i) The slip on the fault plane, which is constrained to be slow slip to avoid seismic wave onset, induces a permanent deformation around the fault plane that may emerge as surface displacement. This permanent seismic

Additional supporting information may be found in the online version of this article.

<sup>1</sup>Institut des Sciences de la Terre (ISTerre), Centre National de la Recherche Scientifique (CNRS), Université de Grenoble, France.

<sup>2</sup>Institut de Recherche pour le Développement (IRD), Lima, Peru.

Corresponding author: L. Tatard, IRD Université de Grenoble CNRS, BP 53, Grenoble Cedex 9, 38041, France. (lucile.tatard@ujf-grenoble.fr)

©2013. American Geophysical Union. All Rights Reserved.  
2169-9313/13/10.1002/jgrb.50215

**Table 1.** Earthquake Databases

Date	Wenchuan 12 May 2008	Chi-Chi 20 Sep 1999	Kashmir 8 Oct 2005	Fiordland 22 Aug 2003	Loma Prieta 18 Oct 1989	Northridge 17 Jan 1994	Rotoehu 18 Jul 2004
$M_w$	7.9	7.6	7.6	7.2	6.9	6.6	5.6
Focal mechanism	thrust	thrust	thrust	thrust	thrust	thrust	normal
Strike-slip component (% of horizontal slip)	33% <sup>a</sup>	10% <sup>c</sup>	4% <sup>f</sup>	None <sup>g</sup>	55% <sup>h</sup>	None <sup>j</sup>	No data
Depth (km)	15 <sup>b</sup>	8 <sup>e</sup>	11 <sup>f</sup>	23 <sup>g</sup>	17 <sup>i</sup>	17 <sup>j</sup>	8 <sup>k</sup>
Depth (km) of upper fault edge	0 <sup>b</sup>	0 <sup>e</sup>	0 <sup>f</sup>	10 <sup>g</sup>	1.5 <sup>i</sup>	5 <sup>j</sup>	7 <sup>k</sup>
Strike (°)	225 <sup>b</sup>	3 <sup>e</sup>	138 <sup>f</sup>	35 <sup>g</sup>	135 <sup>i</sup>	122 <sup>j</sup>	35 <sup>k</sup>
Dip (°)	39 <sup>b</sup>	29 <sup>e</sup>	29 <sup>f</sup>	29 <sup>g</sup>	70 <sup>i</sup>	40 <sup>j</sup>	61 <sup>k</sup>
Rake (°)	120 <sup>b</sup>	66 <sup>e</sup>	140 <sup>f</sup>	95 <sup>g</sup>	135 <sup>i</sup>	101 <sup>j</sup>	no data
$L_{\text{field}}$ (km)	240 <sup>c</sup>	100 <sup>e</sup>	75 <sup>f</sup>	None <sup>g</sup>	None <sup>i</sup>	None <sup>j</sup>	None <sup>k</sup>
$L_{\text{wc}}$ (km)	170 <sup>d</sup>	106 <sup>d</sup>	106 <sup>d</sup>	56 <sup>d</sup>	35 <sup>d</sup>	22 <sup>d</sup>	4 <sup>d</sup>
$L_{\text{inv}}$ (km)	300 <sup>b</sup>	100 <sup>e</sup>	75 <sup>f</sup>	60 <sup>g</sup>	40 <sup>i</sup>	15 <sup>j</sup>	4 <sup>k</sup>
Specificity of mainshock				offshore		10 km away from closest relief	within earthquake swarm

<sup>a</sup>Ren et al. [2010].<sup>b</sup>Zhang et al. [2009].<sup>c</sup>Xu et al. [2009].<sup>d</sup>Wells and Coppersmith [1994].<sup>e</sup>Ma et al. [2001].<sup>f</sup>Avouac et al. [2006].<sup>g</sup>McGinty and Robinson [2007].<sup>h</sup>Kanamori and Satake [1990].<sup>i</sup>Wald et al. [1991].<sup>j</sup>Wald et al. [1996].<sup>k</sup>Hurst et al. [2008].

$L_{\text{field}}$  corresponds to the ruptured fault length measured on the field,  $L_{\text{wc}}$  corresponds to the ruptured fault length calculated from Wells and Coppersmith [1994],  $L_{\text{inv}}$  corresponds to the ruptured fault length given by inversion.

deformation scales, on a given volume, as the product of the surface that slips by the slip value. This product is defined as the earthquake deformation potency [Ben-Zion, 2003, 2008]. (ii) Because the seismic slip occurs with a nonconstant slip velocity, it triggers seismic waves that induce seismic shaking all around the fault. In the near field, i.e., 1 to 5 fault length distance from the earthquake, this severe shaking may induce permanent damage within the rock matrix [Sibson, 2002; Karabulut and Bouchon, 2007]. These seismic waves further propagate away from the seismic fault in the far field.

[5] To understand the role of the earthquake source mechanics on landslide triggering, we investigate seven of the best constrained earthquake-triggered landslide databases with  $M_w=5.6\text{--}7.9$  source sizes, including dip-slip, buried fault earthquakes, oblique-slip earthquakes, and surface-faulting earthquakes. We use the probability distribution functions (PDFs) of the number of triggered landslides relative to the distance to the seismic fault to cross-analyze the seven landslide spatial distributions. Then, in order to compare quantitatively the seven landslide spatial distributions to each other, we normalize the landslide distances to the earthquake fault by the corresponding earthquake ruptured fault length. Once normalized, we analyze how the distributions superpose on each other for each faulting style group. When distributions overlap, i.e., a so-called “data collapse” is achieved, the normalizing parameter (e.g., the amplitude of the earthquake slip in our study) is demonstrated as a control parameter for the studied distributions (e.g., the landslide distances to the fault) [e.g., Stanley, 1987; Barenblatt, 1996]. Our results originally suggest the faulting style (amplitude and rake of seismic slip, surface versus buried fault slip) has a direct role on distance triggering for earthquake-landslide interactions. We then discuss implications for the mechanics of landslide triggering

and for early response to coseismic landslide hazard in mountainous area.

## 2. Data

[6] The seven landslide databases we work with are associated to the  $M_w7.9$  Wenchuan earthquake (China),  $M_w7.6$  Chi-Chi earthquake (Taiwan),  $M_w7.6$  Kashmir earthquake (Pakistan),  $M_w7.2$  Fiordland earthquake (South Island, New Zealand),  $M_w6.9$  Loma Prieta earthquake (California, USA),  $M_w6.6$  Northridge earthquake (California, USA), and  $M_w5.6$  Rotoehu earthquake (North Island, New Zealand). Two events are pure reverse faulting (Fiordland, Northridge), one normal faulting (Rotoehu) and the last four events, the Chi-Chi, Kashmir, Wenchuan, and Loma Prieta earthquakes, have a 4%, 10%, 33%, and 55% of strike-slip component, respectively. The three  $M_w\geq7.6$  earthquakes are surface-faulting earthquake (see Table 1 and Figure S1 for details).

[7] The landslide inventories were set up using either satellite images (Wenchuan, Chi-Chi and Kashmir), or aerial photographs (Fiordland and Northridge), or were set up in the field (Loma Prieta and Rotoehu). The number of mapped landslides varies from 51 (Rotoehu) to more than 60,000 for the Wenchuan database (Figure 1, Table 2, and Figure S1 for details). As the coseismic landslide inventories were set up differently for each event, heterogeneities in the resolutions in space, time, and size of landslide occurrences exist among the seven catalogs.

### 2.1. Location Accuracy

[8] The uncertainty on the landslide location is in the 0.1–2.3 km range and is mainly due to the conversion of a 3-D landslide to a single point, having a single latitude and longitude. The uncertainty is then approximately equal to half the

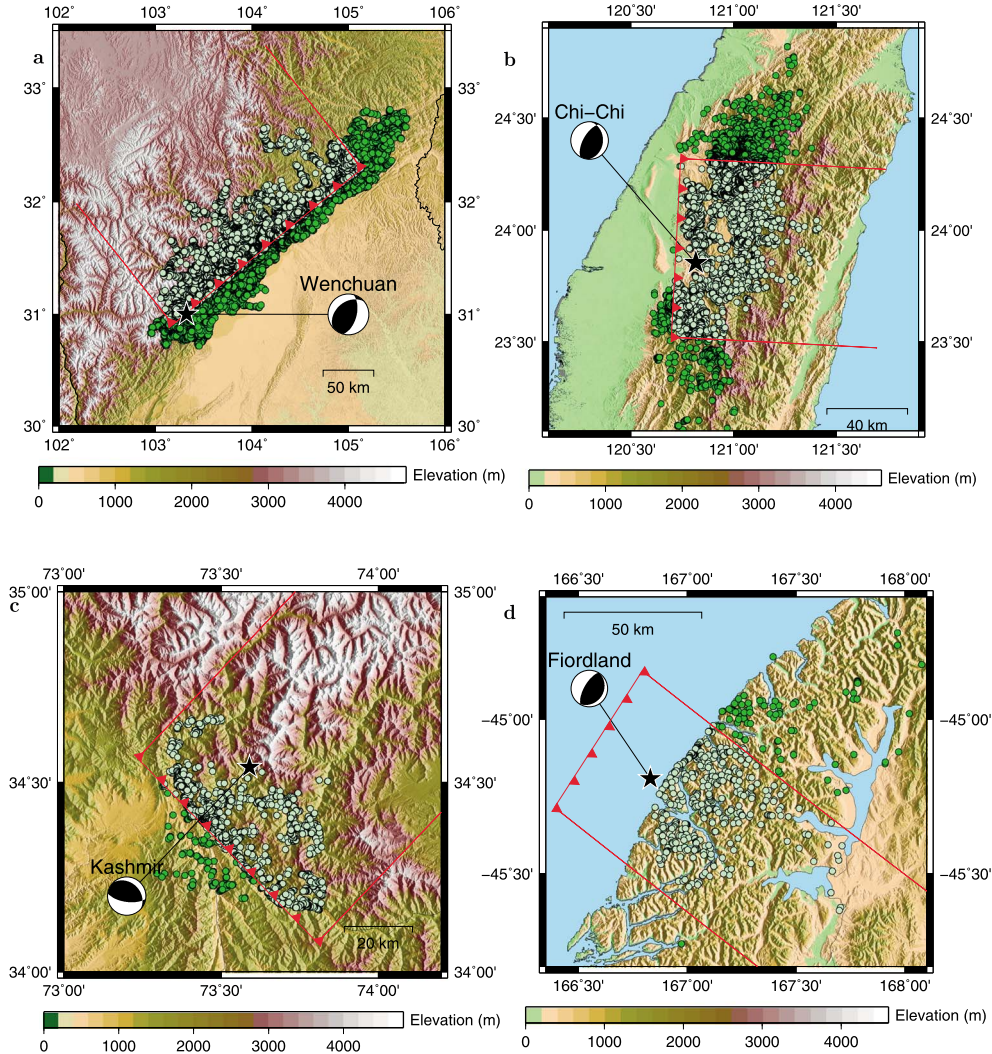


**Figure 1.** Maps of landslides triggered by earthquakes. (a)  $M_w$  7.9 Wenchuan, China event; (b)  $M_w$  7.6 Chi-Chi, Taiwan event; (c)  $M_w$  7.6 Kashmir, Pakistan event; (d)  $M_w$  7.2 Fiordland, New Zealand event; (e)  $M_w$  6.9 Loma Prieta, USA event; (f)  $M_w$  6.6 Northridge, USA event; and (g)  $M_w$  5.6 Rotoehu, New Zealand event. Black star, mainshock epicenter; saw-like red line, surface fault (Figures 1a–1c), vertical projection of fault plane upper edge on the surface (Figures 1d–1g); red lines: definition of hanging wall box. Beach balls are focal solutions from Harvard Centroid Moment Tensor catalog.

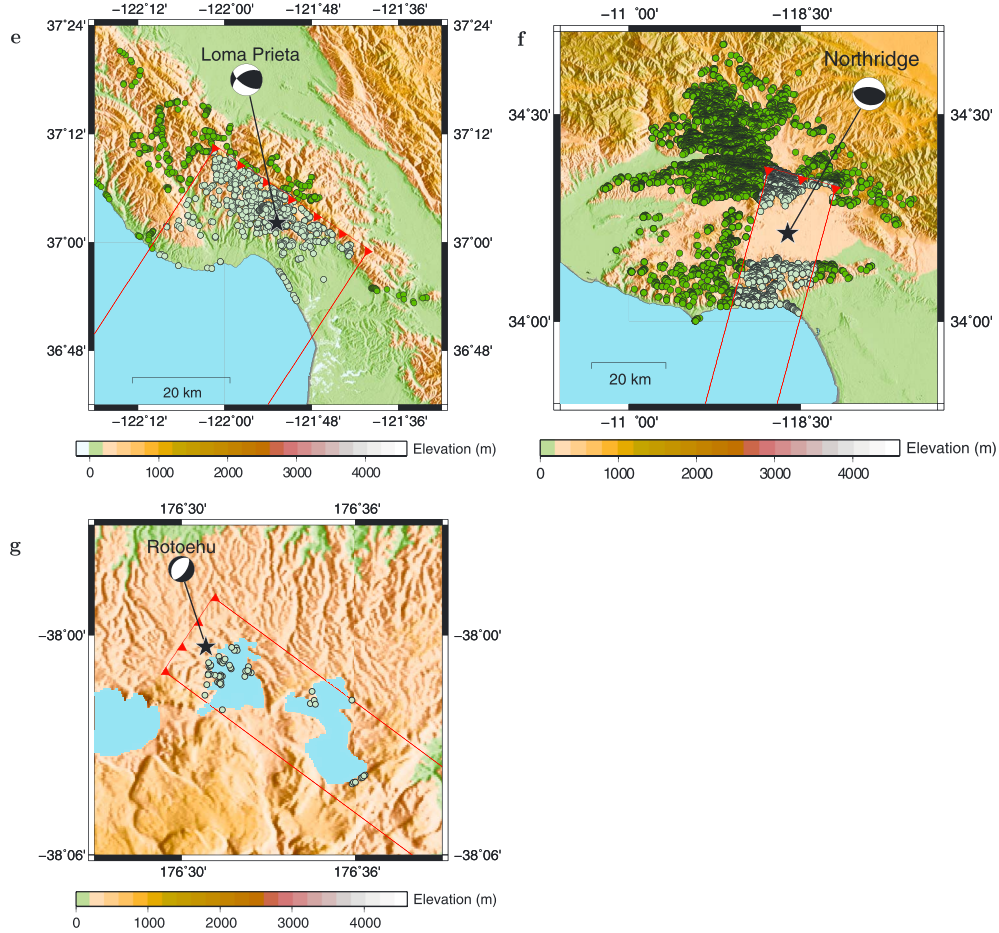
runout distance, and can reach 2.3 km in our databases (see Table 2 and Figure S2 for details). The earthquake-landslide distances are also affected by uncertainty on the location of the seven seismic faults. It corresponds, for the surface rupturing earthquakes, to the difference between the mapped surface fault trace and the linearized one we use, and is approximately equal to 5 km. For the buried earthquakes, the fault location uncertainty depends on the inversion technique used to estimate the fault dimension and is approximately equal to 2 km (see Figure S2 for details).

[9] Another issue when addressing the quality of the landslide inventories is the limitation of the landslide reconnaissance to the area of intense landsliding, i.e., close to the mainshock location. This is well exemplified with the Kashmir inventory, which is limited to the extent of a single SPOT 5 image [Sato *et al.*, 2007]. For the other inventories, too, some landslides that occurred at large distances from the mainshock may have been missed. Indeed, Tatard *et al.* [2010] found earthquake-landslide

interactions at distances as large as 20 times the mainshock fault length. To our knowledge, there is no quantitative evaluation of possible under-sampling at large distances for any of the landslide inventories we used. However, landslide maps from Figure 1 show rough continuous cluster of events, supporting a homogeneous sampling. We checked for all the inventories that the size of these clusters are truncated neither by the lack of available data nor by the lack of topography (see section 4). In this study, we bound our analysis to the spatial pattern of triggered landslides in the near field, i.e., at distance smaller than 1–5 fault length distance from the mainshock. These are also the distances where most of the landslides occurred.

## 2.2. Time Accuracy

[10] The timing of earthquake-triggered landslides depends on the reconnaissance techniques used to build up the inventories. For the four inventories built up using field and airborne inspection (Fiordland, Loma Prieta, Northridge, and Rotoehu),

**Figure 1.** (continued)

the landslide time accuracy is within 1–7 days, as estimated from the time delay between the earthquake occurrence and the landslide reconnaissance (Table 2 and Figure S1). For the three inventories built up using remote sensing techniques (Wenchuan, Chi-Chi, and Kashmir), the time accuracy, which is the delay between the pre-earthquake and postearthquake satellite images, varies from 1 to 7 months (up to several years for some of the 52 Wenchuan satellite images) (Table 2). For all inventories, there is an issue on the respective role of the mainshock and of the following aftershocks in triggering landslides, as there is no instantaneous landslide reconnaissance right after the mainshock occurrence (Table 2). While there are few reports on landslide triggering by aftershocks [e.g., Hung, 2000], we are not aware of any reports of landslides triggered by aftershocks for the seven inventories we study.

### 2.3. Size Accuracy

[11] Another uncertainty in the landslide inventories is related to inaccuracies on discrete landslide identification. Several contiguous events may be mapped as one single event. This uncertainty, although not quantified for the published inventories we used, is independent of the landslide distance to the fault and therefore equally affects the absolute number of landslides at any distance to the fault. For the Fiordland, Loma Prieta, and Rotoehu landslide inventories, there are no or few volume or area estimates (Table 2). This

way, it is not possible to correct the landslide inventories from their respective detection threshold [e.g., Dussauge *et al.*, 2002] nor quantify the completeness of these inventories. While these uncertainties prevent us to compare absolute landslide patterns, we address this problem and minimize the influence of local catalog defects by using probability density functions, rather than discrete distributions, to characterize landslide distance distributions to the earthquake fault (see section 3 for details).

## 3. Method

### 3.1. Data Selection: Hanging Wall Landslides

[12] In order to investigate the role of the earthquake source mechanics on landslide triggering, we restrict our analysis to the landslides that occurred on the hanging wall, where the seismic deformation (transitory and permanent) is the strongest. In effect, (i) the seismic shaking is larger in the hanging wall than in the foot wall due to multiple reflection and wave trapping notably [e.g., Campbell, 2003; Chang *et al.*, 2004], and (ii) the maximum of permanent deformation is located in the hanging wall for dip-slip and oblique-slip earthquakes [e.g., Stein, 1999, for a review]. Ultimately, the landslides we used for analysis are the ones located in the red boxes of Figure 1, whose lateral extent is equal to  $L$ , the length of the fault that ruptured during the earthquake.

**Table 2.** Landslide Databases

	Wenchuan	Chi-Chi	Kashmir	Fiordland	Loma Prieta	Northridge	Rotoehu
Measurement	2.5 to 15 m resolution: ASTER, ALOS, Cartosat-1, SPOT-5, IKONOS <sup>a</sup>	20 m SPOT 5 image <sup>c</sup>	2.5 m SPOT 5 images <sup>e</sup>	Airborne inspection <sup>g</sup>	Field investigation <sup>h</sup>	High-altitude aerial photography (1:60,000) <sup>i</sup>	Airborne and field inspection <sup>j</sup>
Uncertainty on landslide mapping (m)	2.5–15 <sup>a</sup>	20 <sup>c</sup>	2.5 <sup>f</sup>	up to 500 <sup>i</sup>	30 <sup>h</sup>	30 <sup>i</sup>	no data
$\Delta t_{\text{aft}}$ (days)	6 to 250 <sup>a</sup>	6 <sup>c</sup>	12 <sup>e</sup>	3–7 <sup>g</sup>	0 <sup>h</sup>	0 <sup>i</sup>	1–6 <sup>j</sup>
$\Delta t_{\text{bef}}$ (months)	< 1 to 84 <sup>a</sup>	2 <sup>c</sup>	7 <sup>e</sup>				
$N$ landslides	60,104 <sup>a</sup>	9272 <sup>c</sup>	2424 <sup>e</sup>	459 <sup>g</sup>	1705 <sup>h</sup>	11,111 <sup>i</sup>	51 <sup>j</sup>
$V_{\max}$ ( $m^3$ )	$7.4 \cdot 10^8$ <sup>b</sup>	$120 \cdot 10^{10}$ <sup>d</sup>	$80 \cdot 10^6$ <sup>f</sup>	$7 \cdot 10^5$ <sup>g</sup>	$> 27 \cdot 10^6$ <sup>h</sup>	$8 \cdot 10^6$ <sup>i</sup>	$3 \cdot 5 \cdot 10^3$ <sup>j</sup>
$R_{\max}$ (km)	$4.6 \cdot 10^8$ <sup>b</sup>	$4.0 \cdot 10^{10}$ <sup>d</sup>	$1.5 \cdot 10^6$ <sup>f</sup>	$1.2 \cdot 10^5$ <sup>g</sup>	1 <sup>h</sup>	0.45 <sup>i</sup>	0.3 <sup>j</sup>
Data on volume	None	None	None	< 30%	< 60%	None	< 30%
Data on area	100%	100%	100%	< 30%	< 30%	100%	< 30%
Lithology	Heterogeneous <sup>a</sup>	Heterogeneous <sup>c</sup>	Heterogeneous <sup>e</sup>	Coarse crystalline rocks <sup>g</sup>	Moderately cemented crystalline rocks <sup>g</sup>	Weakly cemented clastic sediments <sup>h</sup>	Unconsolidated pyroclastics and tephra deposits <sup>j</sup>

<sup>a</sup>Gorum et al. [2011].<sup>b</sup>Dai et al. [2010].<sup>c</sup>Lin et al. [2003].<sup>d</sup>Hung [2000].<sup>e</sup>Sato et al. [2007].<sup>f</sup>Harp and Crone [2006].<sup>g</sup>Hancox et al. [2003].<sup>h</sup>Keefer et al. [1998] and Keefer [2000].<sup>i</sup>Harp and Jibson [1996].<sup>j</sup>Hancox et al. [2004].

$\Delta t_{\text{aft}}$ , time delay between the mainshock and the landslide reconnaissance (post earthquake image);  $\Delta t_{\text{bef}}$ , time delay between the mainshock and the pre-earthquake image.  $V_{\max}$ ,  $R_{\max}$  volume and runout of the largest landslide of the database.

### 3.2. Distances to Earthquake Fault

[13] In the landslide community, both distances to epicenter and to surface fault trace are used [e.g., Keefer, 2002, and references therein]. Because we investigate the role of the seismic slip on landslide triggering in the near field, it rejects the earthquake as a single point source process. Accordingly, we cannot use distances to either epicenter or hypocenter and use distances  $d$  to the earthquake fault. For surface faulting earthquakes, i.e., the Wenchuan, Chi-Chi and Kashmir events, we define  $d$  as the distance between the landslides and the linearized surface fault trace. For the blind earthquakes whose ruptures did not reach the surface (Fiordland, Loma Prieta, Northridge, and Rotoehu), we define  $d$  as the distance between landslides and the vertical projection of the upper edge of the earthquake fault plane on the surface [Joyner and Boore, 1981; Joyner and Boore, 1988; Bolt and Abrahamson, 2003]. The uncertainties on the fault locations, as derived from seismic and geodetic inversion, are in the 2–5 km range (see Figure S2 for details).

[14] Note that we also used landslide distances to the earthquake fault plane, rather than the earthquake fault trace, and found that it does not impact our results significantly (Figure S3).

### 3.3. Probability Density Function of Triggered Landslide Spatial Distribution

[15] To analyze the seven landslide spatial distributions, we use PDFs corresponding to a density of landslide occurrences per distance bins. They are less sensitive to the lack of calibrated landslide catalogs than discrete functions. We computed the density of the number of landslides using a log binning and a lognormal kernel of width equal to 0.1 [e.g., Izenman, 1991]. We then normalized each bin by the total number of landslides triggered by the earthquake. The

convolution with a lognormal kernel ensures a smoothing of sparse data sets [e.g., Tatard et al., 2010]. The normalization by the total number of landslides allows us to compare all databases, even though the absolute number of landslides within each database spans 3 orders of magnitude (cf. Table 2). For the analysis, we focus on the global shape of the PDF rather than on the small-scale variations. Specifically, we focus on the decrease of the density of triggered landslides.

### 3.4. Collapse of Triggered Landslide Spatial Distributions

[16] In order to (i) robustly compare the seven landslide distributions and (ii) quantify the control of earthquake source parameters on landslide triggering, we normalize the distance distributions by the size of the triggering earthquake. When normalized distributions superpose, i.e., the studied landslide distributions have their landslide decay at similar normalized distance, it demonstrates the key control of the normalizing parameter on the triggering process [e.g., Bak et al., 2002; Tahir et al., 2012]. Because the earthquake fault length  $L$  (the fault length on which coseismic slip is resolved) scales with the earthquake magnitude [e.g., Wells and Coppersmith, 1994; Ben-Zion, 2008], we define the normalized distance as  $d_{wc}^* = d/L_{wc}$ .  $L_{wc}$  is the earthquake fault length derived from  $L_{wc} = 10^{0.59M_w}$  [Wells and Coppersmith, 1994, Table 2A], with  $M_w$  the earthquake moment magnitude.  $L_{wc}$  is the only metrics for fault length values that is available for all of the seven catalogs we use (see Table 1 for values). Field estimates  $L_{\text{field}}$  are available only for the three surface faulting shocks, i.e., the Wenchuan, Chi-Chi, and Kashmir events (Table 1). For all events but the Rotoehu one, inversion estimates for fault lengths  $L_{\text{inv}}$  are also resolved through inversion of seismic and/or GPS records (Table 1). As tests of robustness, we check if our results are stable when using different

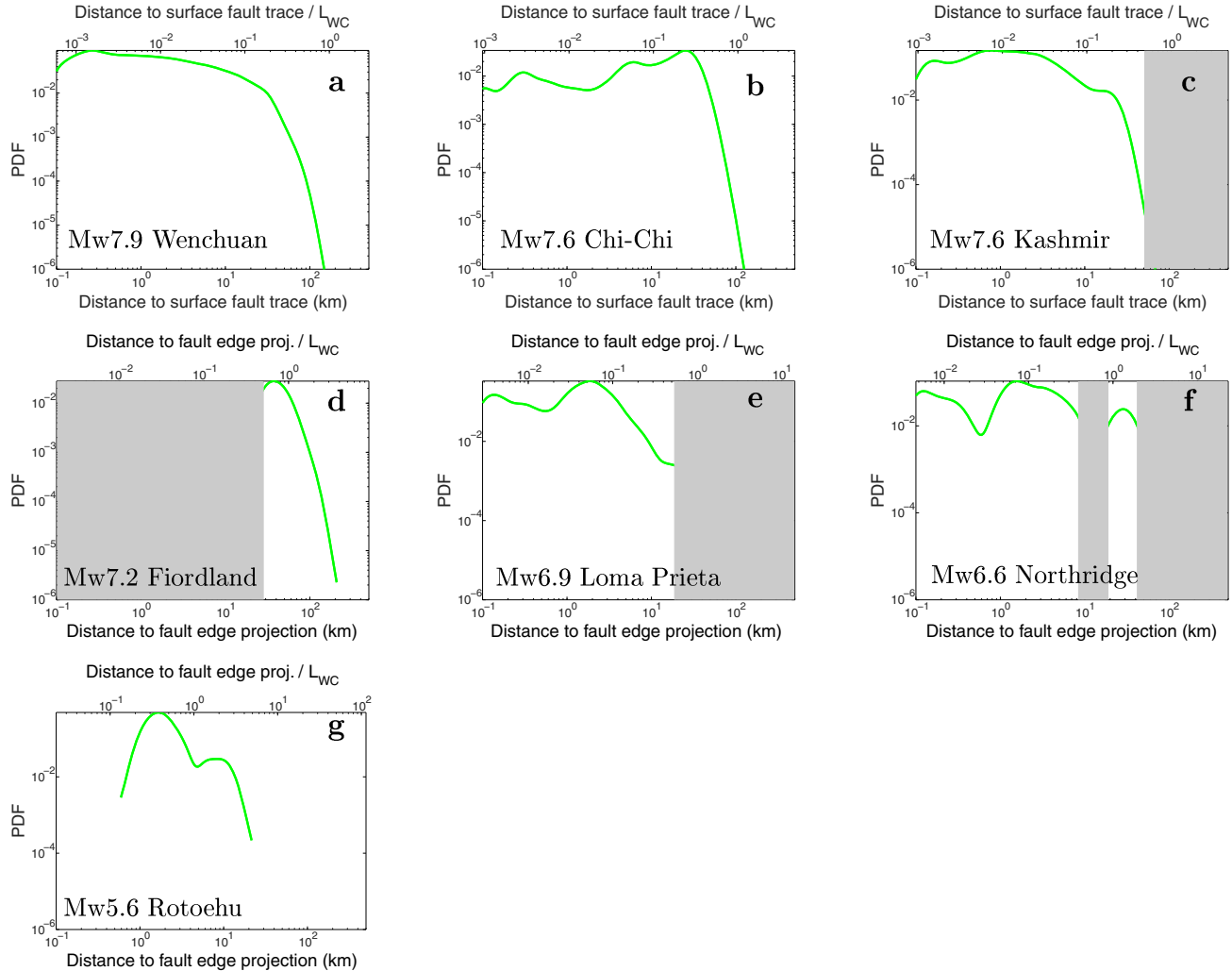


**Figure 2.** Distance distributions to the seismic fault for the landslides on the hanging wall. (a) Wenchuan, (b) Chi-Chi, (c) Kashmir, (d) Fiordland, (e) Loma Prieta, (f) Northridge, and (g) Rotoehu. Distances on the top axis are normalized by  $L_{wc}$ , the mainshock fault length as computed using Wells and Coppersmith [1994] relationship (for details see section 3). The gray shaded rectangles correspond to areas without terrestrial topography (Figure 1, details in Figure S1).

normalized distances such as  $d_{inv}^* = d/L_{inv}$  and  $d_{field}^* = d/L_{field}$ , when values are available (see Figure S4).

[17] To further quantify the comparison among the seven distance distributions of triggered landslides, we define  $d_{95}^*$  and  $d_{75}^*$  as the maximum distances reached by 95 and 75% of the landslides, respectively.

## 4. Results

### 4.1. Characterization of the Seven Landslide Spatial Distributions

[18] The spatial PDFs of the hanging wall landslides are globally described by a rough plateau followed by a decay of landslide density with increasing distance to the seismic fault (Figure 2). The second-order variations on the PDFs are dominated by the availability or lack of inland topography. Because the Fiordland mainshock fault is located  $\sim 20$  km offshore, there is a lack of landslides between 0 and 20 km, as the probable submarine landslides are not reported in the inventory. We test

the influence of the fault location by shifting the hanging wall box eastward or westward and find similar landslide distributions, supporting robust results (Figure S2). For the Northridge event, the local minimum of landslides at 8–20 km from the fault is controlled by the lack of topography within the corresponding distance range. Here also, we test the impact of fault location uncertainties on the landslide PDF. We retrieve similar landslide distributions when shifting the hanging wall box eastward or westward (Figure S2).

[19] We check how the location of the shoreline, located at some 20 and 40 km from the seismic fault for the Loma Prieta and Northridge events, respectively, may control the decrease of the landslide density. For both events, numerous earthquake-triggered landslides cluster on the shoreline (Figure 1). Because the probable submarine landslides are not reported in the inventories, we may miss the largest distances at which landslides were triggered. Nevertheless, for these two events, the onsets of the decrease of the number of landslides occurred at distances significantly smaller than the shoreline distance (Figures 2e and 2f).

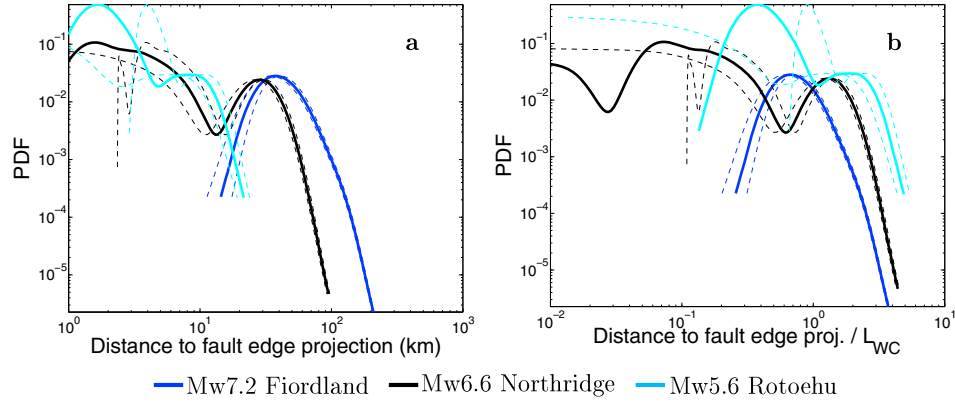


**Figure 3.** Distance distributions of landslides triggered on the hanging wall by the three dip-slip, buried earthquakes. (a) Regular distributions, (b) normalized distance distributions  $d^*_{wc} = d/L_{wc}$ , with  $L_{wc}$  the earthquake fault length as computed using *Wells and Coppersmith* [1994] relationship. Thick lines: landslide distance distributions; thin dashed lines: landslide distance distributions with associated uncertainty (see Figure S2 for values). Note that, for small values of distances, i.e., landslides close to the projected fault trace, the uncertainty value is much larger than the distance to the projected fault trace value. Accordingly, the error bar dives almost vertically for a distance to the fault plane equal to the uncertainty value.

Since we do capture the global decaying pattern of the number of landslides, our databases are validated to study near-field landsliding.

[20] For the Kashmir event, the landslide reconnaissance was performed at maximum distances of 60 km, due to the size of the single SPOT image used for the inventory [*Sato et al.*, 2007]. However, we show that the decrease of the number of landslides with distance to the fault does not overlap with the finite size of the SPOT image (Figures 1c and 2c). The use of this landslide inventory, although set up from a single satellite image, allows us to capture a representative snapshot of the spatial pattern of landslides triggered in the near field and on the hanging wall.

#### 4.2. Role of the Amplitude of the Coseismic Slip on Landslide Spatial Distributions

[21] The three buried  $M_w$  7.2, Fiordland,  $M_w$  6.6 Northridge, and  $M_w$  5.6 Rotoehu earthquakes are pure dip-slip events; they share a similar rake orthogonal to the fault trace. We analyze the 1-D landslide distance distribution using the average coseismic slip over the whole fault plane. Therefore, 2-D slip heterogeneity on the fault planes are not taken into account. The main variation in source processes between the three events is the amplitude of their average coseismic slip values. For these three sequences, the corresponding landslide distance distributions span over 2 orders of magnitude with the maximum triggering distances in the 10 to 100 km range. When normalized by  $L_{wc}$ , the fault length that slipped during the earthquake, the three landslide distance distributions overlap (Figure 3). These distributions give  $0.7 < d^*_{75} < 1.9$  and  $2.9 < d^*_{95} < 4.1$  (Table 3). Since the fault length  $L_{wc}$  for each earthquake scales with the average displacement  $AD_{wc}^\delta$ , with  $\delta \sim 1$  [e.g., *Wells and Coppersmith*, 1994; *Ben-Zion*, 2008], both fault length and average displacement correlate with landslide triggering distances. Because the earthquake potency to deform a given volume is defined as the product of the fault slip by the fault surface [*Ben-Zion*, 2003, 2008], our results

suggest the coseismic deformation may be another control parameter for the spatial occurrence of landslides triggered by dip-slip earthquakes.

[22] Our results support that the change in landslide triggering distances is predicted, as a first-order pattern, by the known scaling relationship between fault length, fault slip, and earthquake magnitude. This way earthquake-triggered landslides emerge as ground failures through inelastic deformation contemporary to the earthquake slip and shaking.

[23] As an attempt to validate the scaling of landslide triggering distances with the magnitude, we analyze the landslides triggered by the  $M_w = 8$ , buried, dip-slip earthquake of Pisco, Peru, of 15 August 2007. This earthquake has a hypocenter depth of 39 km and is representative of thrust faulting from subduction zone [*Sladen et al.*, 2010]. The landslide inventory associated with this earthquake was set up on the field by the Ingemmet, the Peruvian institute in charge of natural hazards, and reports 133 landslides [*Zavala et al.*, 2009]. Using the empirical relationship proposed by *Keefer* [2002], one may expect a larger number of

**Table 3.**  $d^*_{95}$  and  $d^*_{75}$  Normalized Distances for All Earthquakes<sup>a</sup>

Earthquake Focal Mechanism	Catalog	$d^*_{95}$	$d^*_{75}$	$d^*_{95\%-DS}$	$d^*_{75\%-DS}$
Surface-faulting earthquakes	Wenchuan	0.7	0.1	0.4	0.1
	Chi-Chi	0.8	0.2	0.8	0.2
	Kashmir	0.5	0.1	0.4	0.1
	Mean	0.7	0.1	0.5	0.1
Buried, oblique-slip earthquake	Loma Prieta	1.0	0.3	2.3	0.6
Buried, dip-slip earthquakes	Fiordland	3.2	1.9	3.2	1.9
	Northridge	2.9	0.7	2.9	0.7
	Rotoehu	4.1	1.9	4.1	1.9
	Pisco	2.2	1.3	2.2	1.3
	Mean	3.1	1.5	3.1	1.5

<sup>a</sup> $d^*_{95}$  and  $d^*_{75}$  are the distances normalized by LWC at which 95 and 75% of the landslides occurred, respectively.  $d^*_{95\%-DS}$  and  $d^*_{75\%-DS}$  are the distances normalized by LWC and weighted by the strike-slip component of the coseismic slip at which 95 and 75% of the landslides occurred, respectively.

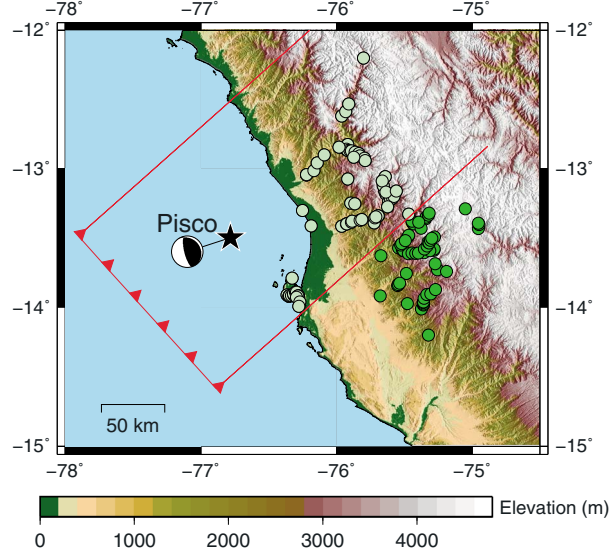


**Figure 4.** Landslides triggered by the  $M_w 8.0$  Pisco earthquake. Black star, mainshock epicenter; saw-like red line, vertical projection of fault plane upper edge on the surface. The fault plane is from Sladen et al. [2010]. Beach ball is the focal mechanism solution from Harvard Centroid Moment Tensor (CMT) catalog.

landslides to be triggered for a  $M_w 8$  earthquake than the observed one. Nevertheless, the landslide distance distribution derived from satellite imaging (P. Lacroix et al., Automatic method for landslide inventories in panchromatic SPOT5 images: application to the earthquake-triggered landslides of Pisco, Peru, 2007,  $M_w 8.0$ , submitted to *Remote Sensing of Environment*, 2013) is similar to the one we retrieved using the field inventory. This way the Ingemmet inventory is one representative sample of the landsliding spatial pattern. Because the Pisco mainshock fault is located some 100 km offshore, and because there is no topography from the coast up to 10 to 30 km inland, there is a lack of landslides at distances between 0 to 130 km to the fault (Figure 4). Adding the Pisco event along with the three other buried, dip-slip events, confirms the landslide spatial

distributions to collapse together, with  $2.2 < d_{95}^* < 4.1$  and  $0.7 < d_{75}^* < 1.9$  (Figure 5b and Table 3). The collapse is achieved for a 2.4 magnitude difference, i.e., fault length in the 4–200 km range. These results support that, for buried, dip-slip earthquakes, the distance at which landslides are triggered is a scale-independent process when normalized by the magnitude of the triggering earthquake.

[24] Similar results are retrieved when normalizing by  $L_{inv}$ , the ruptured fault length calculated from inversion, rather than  $L_{wc}$  (Figure S4), or when using distances to the earthquake fault plane, rather than to the projection of the surface fault trace (Figure S3). Since distance uncertainties are small compared to the distances at which landslide density decreases, its impact is weak on our results. The Rotoehu event, presenting the smallest landslide-earthquake fault distances, is the most affected by the location errors.

#### 4.3. Role of the Coseismic Slip Rake on Landslide Spatial Distributions

[25] To go beyond the impact of the seismic slip amplitude on landslide triggering distances, we isolate the possible role of seismic slip rake on landslide triggering patterns. From Table 3 and Figures 6a and 6b, the Loma Prieta oblique-slip earthquake triggered landslides at shorter distances ( $d_{95}^* = 1.0$  and  $d_{75}^* = 0.3$ ) than the three dip-slip earthquakes ( $2.2 < d_{95}^* < 4.1$  and  $0.7 < d_{75}^* < 1.9$ ). To further isolate the underlying mechanics that may relate the earthquake slip rake to the landslide triggering distances, we define the  $L_{wc} \times \%DS$  normalized distance, i.e.,  $L_{wc}$  is weighted by the percentage of the dip-slip component DS of the earthquake slip. It corresponds to the amount of slip orthogonal to the fault plane. When normalized by  $L_{wc} \times \%DS$ , with  $DS=100\%$  for the dip-slip earthquakes and  $DS=45\%$  for Loma Prieta (Table 1), the distance distributions of landslides triggered by the three blind, dip-slip Fiordland, Northridge, and Rotoehu earthquakes and the Loma Prieta oblique-slip, blind earthquake overlap (Figure 6c). The Loma Prieta normalized output values of  $d_{95-DS}^* = 2.3$  and  $d_{75-DS}^* = 0.6$  are of the same order of magnitude than the distances  $d_{95}^*$  and  $d_{75}^*$  associated with the three dip-slip earthquakes (Table 3). For the same slip values, our result

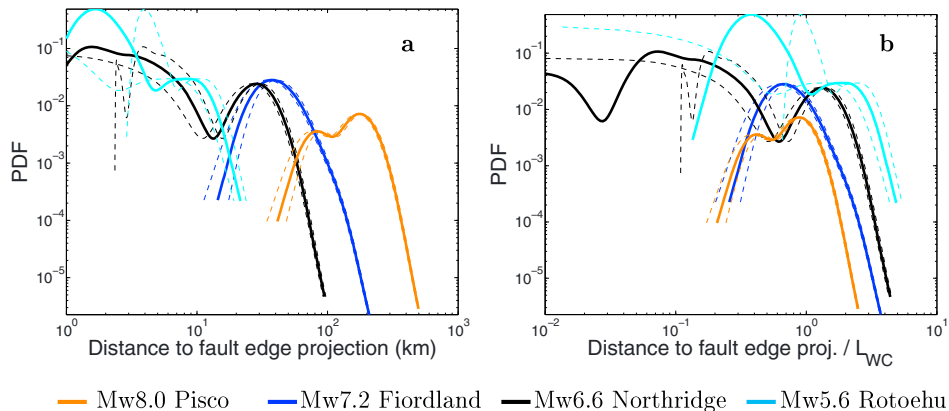


**Figure 5.** Distance distributions for landslides triggered on the hanging wall by the four buried, dip-slip earthquakes. (a) Regular distributions, (b) normalized distance distributions  $\mathbf{d}_{wc} = d/L_{wc}$ , with  $L_{wc}$  the earthquake fault length as computed using Wells and Coppersmith [1994] relationship. See caption of Figure 3 for details.

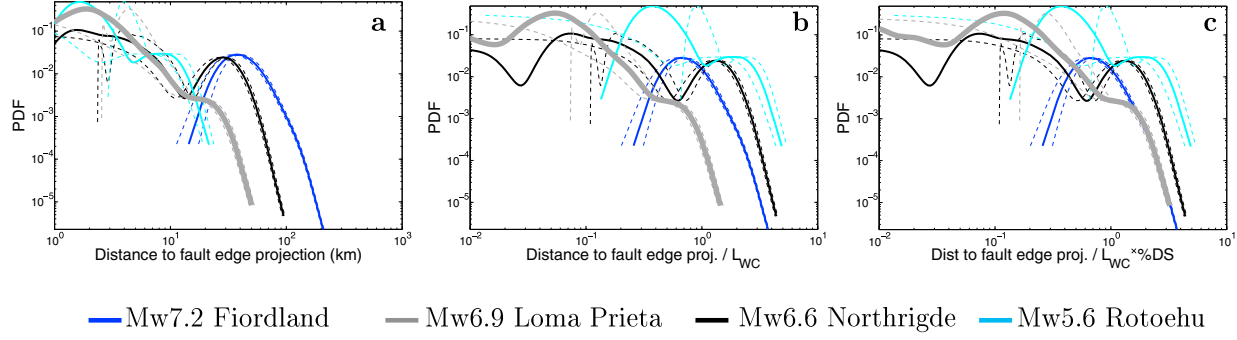


**Figure 6.** Distance distributions of landslides triggered on the hanging wall by the three buried, dip-slip earthquakes and the buried, oblique-slip earthquake. (a) Regular distributions, (b) normalized distance distributions  $d_{wc}^* = d/L_{wc}$ , with  $L_{wc}$  the earthquake fault length as computed using *Wells and Coppersmith [1994]* relationship. (c) Normalized distance distributions  $d_{wc-DS}^* = d/(L_{wc} \times \%DS)$ , with  $\%DS$  the dip-slip component of the earthquake slip in percent. Note that  $\%DS = 100\%$  for the three dip-slip events. Thickest line: landslides triggered by oblique-slip earthquake; thick lines: landslides triggered by pure dip-slip earthquakes; thinnest lines: landslide distance distributions with associated uncertainty (see Figure S2 for values). See caption Figure 3 for details.

argues that oblique-slip earthquakes trigger landslides at shorter distances than the dip-slip earthquakes. This result confirms that the faulting style as measured by the dip-slip component of the earthquake has a role on landslide triggering distances.

[26] Similar results are retrieved when normalizing by  $L_{inv}$ , the ruptured fault length calculated from inversion, rather than  $L_{wc}$  or when using distances to the earthquake fault plane, rather than to the earthquake fault trace. Normalizing the landslide distance distributions by the vertical and the horizontal components of  $AD$ , the average displacement, respectively equal to  $AD \times \sin(dip)$  and  $AD \times \cos(dip)$  did not improve the collapses significantly.

[27] As a key validation of the role of the slip rake on landslide triggering distances, we highlight the landslide pattern triggered by the  $M_w 7.9$  Denali strike-slip earthquake of 3 November 2002. For this earthquake, landslides were reported as “bounded to an unexpectedly narrow 30-km wide band width that straddled the fault-rupture zone over its entire 340-km length” [Eberhart-Phillips *et al.*, 2003;

Jibson *et al.*, 2006]. From our analysis, such an unexpected pattern for an earthquake of this magnitude appears as characteristic of landslide triggering by earthquakes with a strong strike-slip component.

#### 4.4. Surface Faulting, Buried Fault Slip, and Earthquake Triggered Landslide Distribution

[28] For the three  $M_w = 7.6$ , 7.6, and 7.9 surface faulting earthquakes, the decrease of the number of landslides with distance to the surface fault trace collapses at distances smaller than the ones associated with the buried earthquakes, i.e.,  $0.5 < d_{95}^* < 0.8$  and  $0.1 < d_{75}^* < 0.2$  (Figure 7 and Table 3).

[29] When we normalize the seven databases by  $L_{wc} \times \%DS$ , with  $\%DS$  equal to 66, 90, and 96% for the Wenchuan, Chi-Chi, and Kashmir events, respectively, we fail to suppress the gap between the spatial distributions of the landslides triggered by the buried and by the surface-faulting earthquakes (Figure S5). It confirms that the effect of the strike-slip component of these surface faulting earthquakes does not dominate

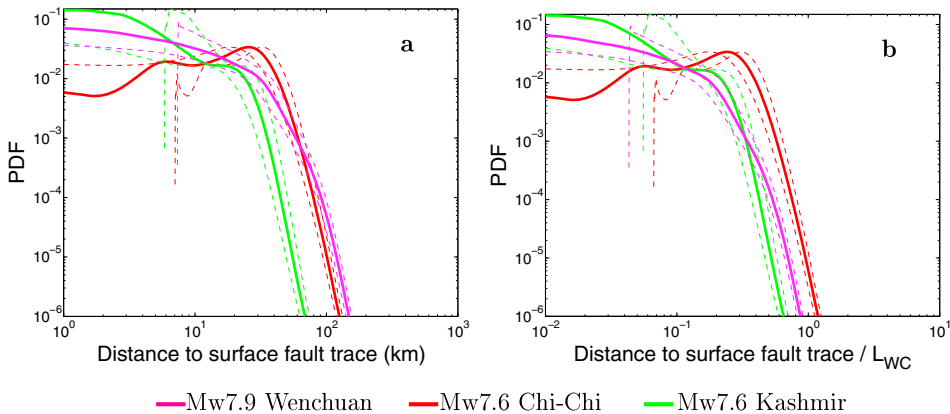


**Figure 7.** Distance distributions of landslides triggered on the hanging wall by the three surface faulting earthquakes. (a) Regular distributions, (b) normalized distance distributions  $d_{wc}^* = d/L_{wc}$ , with  $L_{wc}$  the earthquake fault length as computed using *Wells and Coppersmith [1994]* relationship. See caption of Figure 3 for details.

the landslide distance pattern we observe. From our databases, surface-faulting earthquakes are the least efficient in triggering landslides away from the fault.

[30] Similar results are retrieved when normalizing by  $L_{\text{field}}$ , the ruptured fault length mapped on the field, rather than  $L_{\text{wc}}$  (Figure S4) or when using distances to the earthquake fault plane, rather than to the surface fault trace (Figure S3). Fault and landslide location uncertainties do not impact the landslide-earthquake fault distances significantly (Figure 7). These results support the surface versus buried earthquake slip, apart from its amplitude and rake, to have a role on landslide distance distributions.

[31] As a final note, our analysis argues for the unexpectedly small 30 km landslide triggering distances reported for landslides triggered by the  $M_w 8.0$  strike-slip Denali earthquake [Eberhart-Phillips *et al.*, 2003], to emerge from the combination of both the strong strike-slip component and the surface expression of the earthquake slip.

## 5. Discussion

[32] Our results support that, for a common faulting style, i.e., buried, pure dip-slip earthquakes, the efficiency to trigger a landslide at a given distance, relatively to the size of the earthquake, is within the same order of magnitude for all earthquakes. This result is achieved for fault lengths in the 4–200 km range, i.e.,  $M_w$  5.6–8.0 earthquake magnitudes. When corrected from the earthquake magnitude, each earthquake slip on a given fault plane induces the same deformation field as a function of the distance to the earthquake fault. This result, which emerges from the scaling  $\log(AD) = a + b * \log(L)$  [Wells and Coppersmith, 1994], argues for low-frequency ground motions, e.g., the Peak Ground Displacement values, which also merge the permanent seismic deformation, to have a role on landslide triggering distances. It is to be noted that PGA does not scale with distance to the fault and magnitude the same way displacements do [e.g., Douglas, 2003, for a review]: in the near field, as magnitude increases, PGA values saturate to a constant value.

[33] For pure dip-slip earthquakes, 75% of the landslides are triggered at distances smaller or equal to  $0.7 < d_{75}^* < 1.9$  fault length distances from the fault (Table 3). For the Loma Prieta oblique slip event, 75% of the landslides are triggered at distances smaller or equal to 0.3. To further check the effect of the strike-slip component of the Loma Prieta earthquake in reducing the distances at which landslides are triggered, we test how the distance distribution associated to an equivalent dip-slip Loma Prieta earthquake collapses with the other dip-slip events distance distributions. 75% of landslides are then triggered at distances smaller or equal to  $0.6 L_{\text{wc}}$ , i.e., close to the lower bound of the pure dip-slip triggering distances (Table 3). Our results highlight the role of the coseismic slip amplitude and rake on landslide triggering distances. Bommer *et al.* [2003] and Douglas [2003] reported that dip-slip earthquakes trigger larger high-frequency ground motions such as PGA and PGV (Peak Ground Velocity) in the near field compared to strike-slip earthquakes. Also, for a similar coseismic slip amplitude, the seismic deformation induced by pure dip-slip events is larger in the hanging wall than the seismic deformation of oblique-slip events [e.g., Stein, 1999].

[34] While the surface-rupturing  $M_w \geq 7.6$  Chi-Chi, Kashmir, and Wenchuan earthquakes are the largest events

of our databases, they triggered landslides at smaller distances than those expected from their magnitude, i.e.,  $0.1 < d_{75}^* < 0.2$  fault length (Table 3). On one hand, for the same imposed vertical displacement, the displacement response of the upper crust, as seen as a thin elastic plate, is two times larger and two thirds less diffuse (as estimated from the half-width of the uplift bulge) for surface breaking fault than for buried fault [e.g., Turcotte and Schubert, 2002]. On the other hand, in the near field, Pitarka *et al.* [2009] reported that buried earthquakes trigger larger ground motions than surface-faulting earthquakes.

[35] The case of the “unexpectedly narrow 30 km width distance from the fault plane for landslide triggered by the Denali earthquake” [Eberhart-Phillips *et al.*, 2003] is rationalized, from our results, as the direct cumulative effect of a strike-slip component and surface-faulting slip for this earthquake. Our analysis suggests that, for a given earthquake size, both the oblique-slip and the surface-faulting slip reduce the distance potency in landslide triggering. It further supports the seismic slip as an additional control parameter for landslide triggering distances.

[36] During the earthquake faulting, the slip duration, i.e., the time on which the seismic slip is completed, may last up to a few tens of seconds for the largest shock [e.g., Singh *et al.*, 2003]. Because of uncertainties on landslide timing (see Table 2), we cannot further identify whether the duration on which the seismic deformation is applied is important for landslide triggering. Accordingly, the question on the relative contribution of the seismic deformation and seismic deformation rate on the triggering of landslides remains an open question. It questions the relative role of PGD, PGV, and PGA on landslide triggering.

[37] As a final note, our results support that, in the near field, the faulting style (amplitude, rake, surface versus buried slip) influences the landslide triggering process during earthquake shaking. In the far field, i.e., at distances larger than 10 fault lengths, there is no reported evidence of the role of slip patterns and faulting style on landslide triggering [e.g., Delgado *et al.*, 2011]. Landslides triggered at these large distances relatively to the one expected from the magnitude of the earthquake trigger can be defined as far-field triggered landslides [e.g., Tatard *et al.*, 2010; Delgado *et al.*, 2011; Jibson and Harp, 2012].

[38] Apart from this near-field/far-field conceptual framework to analyze landslide triggering, our results provide distances to fault trace or surface projection of the fault within which 75–95% of landslides are located, depending on the earthquake faulting style. It refines the maximum distance envelope for landslide triggering previously proposed by Wilson and Keefer [1985] as soon as the earthquake focal mechanism is available. Additional inventories are mandatory to be able to refine how earthquake source properties control landslide triggering.

## 6. Conclusions

[39] In order to understand how seismic source properties may control the distance distribution of earthquake-triggered landslides, we grouped the landslide databases as a function of the faulting mechanism of the trigger earthquake. First, we showed landslide distances distributions triggered by dip-slip, buried,  $M5.6$ – $7.2$  earthquakes, i.e., the Rotoehu, Northridge, and Fiordland events, collapse together once

the distances are normalized by the ruptured fault length  $L$  of the trigger earthquake. This result supports the coseismic deformation, through the earthquake slip amplitude, as another controlling parameter of landslide triggering distances. The collapse is robust when adding the  $M_w 8.0$  dip-slip, buried event of Pisco, Peru. Second, the buried, oblique-slip earthquake of our database, i.e., the Loma Prieta event, triggered landslides at shorter normalized distances than the landslides triggered by the three dip-slip, buried earthquakes. When normalized by the dip-slip component of the earthquake slip, the landslide distance distributions of these four buried earthquakes collapse. This result argues for the earthquake slip rake to have a role on landslide triggering distances. Third, the landslides triggered by the three  $M_w 7.9, 7.6, 7.6$  surface faulting earthquakes (Wenchuan, Chi-Chi, Kashmir), were triggered at normalized distances smaller than the ones expected from their magnitude. This result highlights the surface versus buried faulting to be a third parameter of the seismic source that controls landslide triggering distances. All these results are robust when using a different proxy for both the normalized distance ( $L_{inv}$ , the earthquake fault size from geophysical inversions,  $L_{wc}$  from Wells and Coppersmith empirical relationship) and the distance to earthquake fault (distance to the earthquake fault plane, distance to the earthquake fault trace). In terms of coseismic landslide management in mountainous areas, our results allow us to propose distances at which 95 and 75% of landslides will be triggered, as a function of three coseismic slip patterns (amplitude, rake, and buried versus surface slip). These normalized distances are equal to  $2.2 < d_{95}^* < 4.1$  and  $0.7 < d_{75}^* < 1.9$  for buried, dip-slip earthquakes and  $0.5 < d_{95}^* < 0.8$  and  $0.1 < d_{75}^* < 0.2$  for surface-slip earthquakes. As soon as the earthquake focal mechanism is available, it would allow the rescue team to focus on the potentially most damaged areas.

[40] **Acknowledgments.** The authors were supported by the French ANR SLAMS project. This paper benefited a lot from discussion with many of the scientists who attended the International Conference in Commemoration of the 10th Anniversary of the 1999 Chi-Chi earthquake. The authors thank C. Voisin, A. Helmstetter, S. Garambois, F. Cotton, C. Van Westen, T. Gorum, X. Fan, Q. Xu, D. Petley, R. Parker and E. Harp for fruitful discussions. They are also very grateful to S. Dellow, T. Gorum, D. Keefer, R. Jibson, J. Michael, H. Sato, L. Fidel, and B. Zavala for sharing the coseismic landslide databases. The comments of several anonymous reviewers and the associated editor on several previous versions of this manuscript greatly clarified it.

## References

- Avouac, J. P., F. Ayoub, S. Leprince, O. Konca, and D. V. Helmberger (2006), The 2005, Mw 7.6 Kashmir earthquake: Sub-pixel correlation of ASTER images and seismic waveforms analysis, *Earth Planet. Sci. Lett.*, 249(3-4), 514–528.
- Bak, P., K. Christensen, L. Danon, and T. Scanlon (2002), Unified scaling law for earthquakes, *Phys. Rev. Lett.*, 88(17), 178501.
- Barenblatt, G. I. (1996), *Scaling, Self-Similarity, and Intermediate Asymptotics*, vol. 14, Cambridge University Press, Cambridge, U.K.
- Ben-Zion, Y. (2003), Appendix 2 key formulas in earthquake seismology, *Int. Geophys.*, 81, 1857–1875.
- Ben-Zion, Y. (2008), Collective behavior of earthquakes and faults: Continuum-discrete transitions, progressive evolutionary changes, and different dynamic regimes, *Rev. Geophys.*, 46, RG4006, doi:10.1029/2008RG000260.
- Bolt, B. A., and N. A. Abrahamson (2003), Estimation of strong seismic ground motions, *Int. Geophys.*, 81, 983–1001.
- Bommer, J., J. Douglas, and F. Strasser (2003), Style-of-faulting in ground motion prediction equations, *Bull. Earthquake Eng.*, 1(2), 171–203.
- Campbell, K. W. (2003), 60. strong-motion attenuation relations, *Int. Geophys.*, 81, 1003–1012.
- Chang, T. Y., F. Cotton, Y. B. Tsai, and J. Angelier (2004), Quantification of hanging-wall effects on ground motion: some insights from the 1999 Chi-Chi earthquake, *Bull. Seismol. Soc. Am.*, 94(6), 2186–2197.
- Dadson, S. J., et al (2004), Earthquake-triggered increase in sediment delivery from an active mountain belt, *Geology*, 32(8), 733.
- Dai, F. C., C. Xu, X. Yao, L. Xu, X. B. Tu, and Q. M. Gong (2010), Spatial distribution of landslides triggered by the 2008 Ms 8.0 Wenchuan earthquake, China, *J. Asian Earth Sci.*, 40, 883–895.
- Delgado, J., J. Garrido, C. López-Casado, S. Martino, and J. A. Peláez (2011), On far field occurrence of seismically induced landslides, *Eng. Geol.*, 123(3), 204–213.
- Douglas, J. (2003), Earthquake ground motion estimation using strong-motion records: a review of equations for the estimation of peak ground acceleration and response spectral ordinates, *Earth Sci. Rev.*, 61(1), 43–104.
- Dussauge, C., A. Helmstetter, J. R. Grasso, D. Hantz, P. Desvarieux, M. Jeannin, and A. Giraud (2002), Probabilistic approach to rock fall hazard assessment: potential of historical data analysis, *Nat. Hazards Earth Syst. Sci.*, 2, 15–26.
- Eberhart-Phillips, D., et al. (2003), The 2002 Denali fault earthquake, Alaska: a large magnitude, slip-partitioned event, *Science*, 300(5622), 1113–1118.
- Gorum, T., X. Fan, C. J. van Westen, R. Q. Huang, Q. Xu, C. Tang, and G. Wang (2011), Distribution pattern of earthquake-induced landslides triggered by the 12 May 2008 Wenchuan earthquake, *Geomorphology*, 133, 152–167.
- Hancox, G. T., S. Cox, I. M. Turnbull, and M. J. Crozier (2003), Reconnaissance studies of landslides and other ground damage caused by the Mw 7.2 Fiordland earthquake of 22 August 2003. Institute of Geological and Nuclear Sciences science report 2003/30.
- Hancox, G. T., D. Dellow, M. Mc Saveney, B. Scott, and P. Villamor (2004), Reconnaissance studies of landslides caused by the  $M_L 5.4$  Lake Rotoehu earthquake and swarm of July 2004. Institute of Geological & Nuclear Sciences science report 2004/24 21p.
- Harp, E. L., and A. J. Crone (2006), Landslides triggered by the October 8, 2005, Pakistan earthquake and associated landslide-dammed reservoirs. *US Geological Survey Open-file Report*, 1052.
- Harp, E. L., and R. W. Jibson (1996), Landslides triggered by the 1994 Northridge, California, earthquake, *Bull. Seismol. Soc. Am.*, 86(1B), S319.
- Hung, J. J. (2000), Chi-Chi earthquake induced landslides in Taiwan, *Earthquake Eng. Eng. Seismol.*, 2(2), 25–33.
- Hurst, T., S. Bannister, R. Robinson, and B. Scott (2008), Characteristics of three recent earthquake sequences in the Taupo Volcanic Zone, New Zealand, *Tectonophysics*, 452, 17–28.
- Izenman, A. J. (1991), Recent developments in nonparametric density estimation, *J. Am. Stat. Assoc.*, 205–224.
- Jibson, R. W., and E. L. Harp (2012), Extraordinary distance limits of landslides triggered by the 2011 Mineral, Virginia, earthquake, *Bull. Seismol. Soc. Am.*, 102(6), 2368–2377.
- Jibson, R. W., E. L. Harp, W. Schulz, and D. K. Keefer (2006), Large rock avalanches triggered by the M 7.9 Denali Fault, Alaska, earthquake of 3 November 2002, *Eng. Geol.*, 83(1), 144–160.
- Jinhui, Y., C. Jie, X. XiWei, W. Xulong, and Z. Yonggang (2010), The characteristics of the landslides triggered by the Wenchuan Ms 8.0 earthquake from Anxian to Beichuan, *J. Asian Earth Sci.*, 37, 452–459.
- Joyner, W. B., and D. M. Boore (1981), Peak horizontal acceleration and velocity from strong-motion records including records from the 1979 Imperial Valley, California, earthquake, *Bull. Seismol. Soc. Am.*, 71(6), 2011–2038.
- Joyner, W. B., and D. M. Boore (1988), Measurement, characterization, and prediction of strong ground motion. In *Earthquake Engineering and Soil Dynamics II, Proceedings of the American Society of Civil Engineers, Geotechnical Engineering Division, Specialty Conference*, pages 27–30.
- Kamp, U., B. J. Growley, G. A. Khattak, and L. A. Owen (2008), GIS-based landslide susceptibility mapping for the 2005 Kashmir earthquake region, *Geomorphology*, 101, 631–642.
- Kanamori, H., and K. Satake (1990), Broadband study of the 1989 Loma Prieta earthquake, *Geophys. Res. Lett.*, 17(8), 1179–1182.
- Karabulut, H., and M. Bouchon (2007), Spatial variability and non-linearity of strong ground motion near a fault, *Geophys. J. Int.*, 170(1), 262–274.
- Keefer, D. K. (2000), Statistical analysis of an earthquake-induced landslide distribution - the 1989 Loma Prieta, California event, *Eng. Geol.*, 58(3-4), 231–249.
- Keefer, D. K. (2002), Investigating landslides caused by earthquakes - a historical review, *Surv. Geophys.*, 23, 573–510.
- Keefer, D. K., G. B. Griggs, and E. L. Harp (1998), Large landslides near the San Andreas fault in the Summit Ridge area, Santa Cruz Mountains, California. *US Geological Survey professional paper*, (1551C).
- Khazai, B., and N. Sitar (2004), Evaluation of factors controlling earthquake-induced landslides caused by Chi-Chi earthquake and comparison with the Northridge and Loma Prieta events, *Eng. Geol.*, 71(1-2), 79–95.
- Lee, C. T. (2010), Re-evaluation of factors controlling earthquake-induced landslides based on new Chi-Chi landslide inventory and high resolution

- DEM. In EGU General Assembly, editor, *Geophysical Research Abstracts*, volume 12.
- Lin, C. W., C. L. Shieh, B. D. Yuan, Y. C. Shieh, S. H. Liu, and S. Y. Lee (2003), Impact of Chi-Chi earthquake on the occurrence of landslides and debris flows: example from the Chhenyulan River watershed, Nantou, Taiwan, *Eng. Geol.*, **71**, 49–61.
- Ma, K. F., J. Mori, S. J. Lee, and S. B. Yu (2001), Spatial and temporal distribution of slip for the 1999 Chi-Chi, Taiwan, earthquake, *Bull. Seismol. Soc. Am.*, **91**(5), 1069–1087.
- McGinty, P., and R. Robinson (2007), The 2003 Mw 7.2 Fiordland subduction earthquake, New Zealand: aftershock distribution, main shock fault plane and static stress changes on the overlying Alpine Fault, *Geophys. J. Int.*, **169**(2), 579–592.
- Meunier, P., N. Hovius, and A. J. Haines (2007), Regional patterns of earthquake-triggered landslides and their relation to ground motion, *Geophys. Res. Lett.*, **34**, L20408, doi:10.1029/2007GL031337.
- Murphy, W., D. N. Petley, J. Bommer, and J. M. Mankelow (2002), Uncertainty in ground motion estimates for the evaluation of slope stability during earthquakes, *Q. J. Eng. Geol. Hydrol.*, **35**(1), 71–78.
- Parise, M., and R. W. Jibson (2000), A seismic landslide susceptibility rating of geologic units based on analysis of characteristics of landslides triggered by the 17 January, 1994 Northridge, California earthquake, *Eng. Geol.*, **58**(3), 251–270.
- Pitarka, A., L. A. Dalguer, S. M. Day, P. G. Somerville, and K. Dan (2009), Numerical study of ground-motion differences between buried-rupturing and surface-rupturing earthquakes, *Bull. Seismol. Soc. Am.*, **99**(3), 1521.
- Ren, J., G. Chen, X. Xu, S. Zhang, and C. Mao (2010), Surface rupture of the 2008 Wenchuan, China, earthquake in the Qingping Stepover determined from geomorphologic surveying and excavation, and its tectonic implications, *Bull. Seismol. Soc. Am.*, **100**(5B), 2651–2659.
- Sato, H. P., H. Hasegawa, S. Fujiwara, M. Tobita, M. Koarai, H. Une, and J. Iwashashi (2007), Interpretation of landslide distribution triggered by the 2005 Northern Pakistan earthquake using SPOT 5 imagery, *Landslides*, **4**(2), 113–122.
- Sepúlveda, S. A., W. Murphy, and D. N. Petley (2005), Topographic controls on coseismic rock slides during the 1999 Chi-Chi earthquake, Taiwan, *Q. J. Eng. Geol. Hydrol.*, **38**(2), 189–196.
- Sibson, R. H. (2002), 29. Geology of the crustal earthquake source, *Int. Geophys.*, **81**, 455–473.
- Singh, S. K., M. Ordaz, and J. F. Pacheco (2003), 66. advances in seismology with impact on earthquake engineering, *Int. Geophys.*, **81**, 1081–1095.
- Sladen, A., H. Tavera, M. Simons, J. P. Avouac, A. O. Konca, H. Perfettini, L. Audin, E. J. Fielding, F. Ortega, R. Cavagnoud (2010), Source model of the 2007 Mw 8.0 Pisco, Peru earthquake: Implications for seismogenic behavior of subduction megathrusts, *J. Geophys. Res.*, **115**, B02405, doi:10.1029/2009JB006429.
- Stanley, H. E. (1987), Introduction to phase transitions and critical phenomena, in *Introduction to Phase Transitions and Critical Phenomena*, edited by H. Eugene Stanley, 336 pp., Oxford University Press, Oxford, U.K.
- Stein, R. S. (1999), The role of stress transfer in earthquake occurrence, *Nature*, **402**(6762), 605–609.
- Tahir, M., J. R. Grasso, and D. Amorèse (2012), The largest aftershock: How strong, how far away, how delayed?, *Geophys. Res. Lett.*, **39**, L04301, doi:10.1029/2011GL050604.
- Tatard, L., J. R. Grasso, A. Helmstetter, and S. Garambois (2010), Characterization and comparison of landslide triggering in different tectonic and climatic settings, *J. Geophys. Res.*, **115**, F04040, doi:10.1029/2009JF001624.
- Turcotte, D. L., and G. Schubert (2002), *Geodynamics*, 456 pp., Cambridge University Press, Cambridge, U.K.
- Wald, D. J., D. V. Helmberger, and T. H. Heaton (1991), Rupture model of the 1989 Loma Prieta earthquake from the inversion of strong-motion and broadband teleseismic data, *Bull. Seismol. Soc. Am.*, **81**(5), 1540–1572.
- Wald, D. J., T. H. Heaton, and K. W. Hudnut (1996), The slip history of the 1994 Northridge, California, earthquake determined from strong-motion, teleseismic, GPS, and leveling data, *Bull. Seismol. Soc. Am.*, **86**(1B), S49.
- Wells, D. L., and K. J. Coppersmith (1994), New empirical relationships among magnitude, rupture length, rupture width, rupture area, and surface displacement, *Bull. Seismol. Soc. Am.*, **84**(4), 974–1002.
- Wilson, R. C., and D. K. Keefer (1985), Predicting areal limits of earthquake-induced landsliding, *Evaluating Earthquake Hazards in the Los Angeles Regime*, US Geological Survey Professional Paper, 1360: 317–345.
- Xu, X., X. Wen, G. Yu, G. Chen, Y. Klinger, J. Hubbard, and J. Shaw (2009), Coseismic reverse-and oblique-slip surface faulting generated by the 2008 Mw 7.9 Wenchuan earthquake, China, *Geology*, **37**(6), 515–518.
- Zavalá, B., R. Hermanns, P. Valderrama, C. Costa, and M. Rosado (2009), Procesos geológicos e intensidad macrosísmica Inqua del sismo de Pisco del 15/08/2007, Perú, *Revista de la Asociación Geológica Argentina*, **65**(4), 760–779.
- Zhang, Y., W. P. Feng, L. S. Xu, C. H. Zhou, and Y. T. Chen (2009), Spatio-temporal rupture process of the 2008 great Wenchuan earthquake, *Sci. China Earth Sci.*, **52**(2), 145–154.